SIMULATING THE OCEAN'S CHLOROPHYLL DYNAMIC RANGE FROM COASTAL UPWELLING TO OLIGOTROPHY

N. Van Oostende[1,*], R. Dussin[2], C. A. Stock[3], A. D. Barton[4], E. Curchitser[2], J. P. Dunne[3] and B. B. Ward[1]

[1] Department of Geosciences, Princeton University, New Jersey, USA

[2] Department of Environmental Sciences, Rutgers University, New Jersey, USA

[3] Geophysical Fluid Dynamics Laboratory, National Oceanic and Atmospheric Administration, Princeton, New Jersey, USA

[4] Scripps Institution of Oceanography and Section of Ecology, Behavior and Evolution, University of California San Diego, USA

**corresponding author*: E-mail: oostende@princeton.edu; Address: 158 Guyot Hall, Princeton University, Princeton NJ 08544, USA

Highlights

- models challenged to simulate full range of global ocean chlorophyll concentrations
- two-phytoplankton size class model captures regional meso- to oligotrophic transition
- adding coastal diatom enables simulation of high chlorophyll in coastal upwelling
- high chlorophyll arises from weaker top-down control and transient trophic decoupling
- new model improves simulated distribution of coastal hypoxia

1 Abstract

The measured concentration of chlorophyll *a* in the surface ocean spans four orders of magnitude, from ~0.01 mg m^{-3} in the oligotrophic gyres to >10 mg m^{-3} in coastal zones. Productive regions encompass only a small fraction of the global ocean area yet they contribute disproportionately to marine resources and biogeochemical processes, such as fish catch and coastal hypoxia. These regions and/or the full observed range of chlorophyll concentration,

however, are often poorly represented in global earth system models (ESMs) used to project climate change impacts on marine ecosystems. Furthermore, recent high resolution (~10 km) global earth system simulations suggest that this shortfall is not solely due to coarse resolution (~100 km) of most global ESMs. By integrating a global biogeochemical model that includes two phytoplankton size classes (typical of many ESMs) into a regional simulation of the California Current System (CCS) we test the hypothesis that a combination of higher spatial resolution and enhanced resolution of phytoplankton size classes and grazer linkages may enable global ESMs to better capture the full range of observed chlorophyll. The CCS is notable for encompassing both oligotrophic (<0.1 mg m^{-3}) and productive (>10 mg m^{-3}) endpoints of the global chlorophyll distribution. As was the case for global high-resolution simulations, the regional high-resolution implementation with two size classes fails to capture the productive endpoint. The addition of a third phytoplankton size class representing a chain-forming coastal diatom enables such models to capture the full range of chlorophyll concentration along a nutrient supply gradient, from highly productive coastal upwelling systems to oligotrophic gyres. Weaker 'top-down' control on coastal diatoms results in stronger trophic decoupling and increased phytoplankton biomass, following the introduction of new nutrients to the photic zone. The enhanced representation of near-shore chlorophyll maxima allows the model to better capture coastal hypoxia along the continental shelf of the North American west coast and may improve the representation of living marine resources.

Keywords: chlorophyll; coastal upwelling; diatom; coastal hypoxia; phytoplankton community size-structure; California Current

2 Introduction

The distribution of phytoplankton exhibits both intricate fine-scale structure and large-scale patterns that shape marine resource distributions and biogeochemical cycles across spatial scales ranging from hundreds of meters to ocean basins (Longhurst 2007; Lévy et al. 2012; Stukel et al. 2017). The measured distribution of chlorophyll, a proxy for phytoplankton biomass, in the open oceans spans four orders of magnitude, ranging from as low as ~0.01 mg m^{-3} in the oligotrophic gyres to more than 10 mg m^{-3} in a few highly productive coastal zones. Oligotrophic subtropical gyres account for the majority of ocean surface area (Longhurst et al. 1995). In contrast, regions

with an annual mean chlorophyll concentration >3 mg m^{-3}, primarily in coastal zones, account for only ~1% of the global ocean (SeaWiFS Level-3 Mapped Chlorophyll Data Version 2014), yet have a disproportionate impact on marine resources and biogeochemical processes. Fish catch, for example, is strongly skewed toward high chlorophyll coastal regions (Ryther 1969; Friedland et al. 2012; Stock et al. 2017). The biological pump is also intensified (Eppley and Peterson 1979; Dunne et al. 2005) and decomposition of sinking organic matter depletes oxygen in zones underlying high productivity. Such regions often harbor unique biogeochemical transformations, such as denitrification (Christensen et al. 1987; DeVries et al. 2012), or hypoxia detrimental to demersal fish and benthic invertebrates (Grantham et al. 2004; Chan et al. 2008; Keller et al. 2015).

The biomass of large phytoplankton (>20 µm), including many species of diatoms, characteristically makes up an important fraction of high biomass phytoplankton blooms (Chisholm 1992; Raimbault et al. 1988; Chavez 1989; Irigoien et al. 2004; Goericke 2011). Moreover, because large phytoplankton dominate at high chlorophyll concentrations, variability in their biomass explains most of the absolute variability in chlorophyll concentration globally (Claustre 1994; Venrick 2002; Uitz et al. 2010). The explanation for this relationship between chlorophyll concentration and contribution of large phytoplankton cells hinges upon the balance of phytoplankton growth and losses to predation. At least two non-mutually exclusive mechanisms have been proposed to explain these observations. The first mechanism is the size-dependent 'sequential invasion' of phytoplankton groups along a resource gradient (cf. Armstrong 1994; Ward et al. 2012). In the steady state case, phytoplankton species of incrementally larger cell size are added sequentially along a gradient of increasing flux of limiting resources (i.e., nutrients), supporting higher autotrophic biomass (Chisholm 1992; Moloney and Field 1989; Irwin et al. 2006; Barber and Hiscock 2006). The smallest phytoplankton cells thrive in low nutrient conditions due to nutrient scavenging advantages afforded by high surface area to volume ratios, and their lower minimal cellular nutrient requirement. As the level of the limiting nutrient increases the abundance of the smallest cells (i.e., picoplankton such as *Prochlorococcus*) is constrained by a grazer-imposed threshold (~0.5 mg chlorophyll m^{-3}), above which the total community biomass is supplemented by increasing

contributions of sequentially larger phytoplankton size groups until the next size-group threshold is reached.

The second mechanism is transient decoupling of phytoplankton biomass accumulation from grazing (Thingstad 1998; Irigoien et al. 2005; Romagnan et al. 2015). This mechanism is often associated with changes from unfavorable to favorable phytoplankton growth conditions, such as spring bloom initiation or the surfacing of upwelled, high nutrient water masses. Microzooplankton growth rates are generally comparable to those of their phytoplankton prey, which allows them to respond rapidly to increases in phytoplankton growth. The high microzooplankton turnover rate can quickly re-establish top-down control on small phytoplankton by cropping a significant portion (averaging 60-75%) of the daily phytoplankton production across a spectrum of ocean and coastal systems (Landry and Calbet 2004). Mesozooplankton, however, grow more slowly and in many cases have longer and more complex life cycles (Hansen et al. 1997), such that their larger phytoplankton prey can temporarily outpace grazer control (Franks 2001; Fuchs and Franks 2010). Because the phytoplankton species dominating at high biomass are typically large, and often mechanically or chemically protected (e.g., dinoflagellates such as *Karenia* sp., *Phaeocystis* spp. colonies, chain-forming diatoms such as *Chaetoceros* spp. and *Thalassiosira* spp.) they are less susceptible to microzooplankton grazing and most vulnerable to larger grazers (Irigoien et al. 2004; Slaughter et al. 2006). This trade-off between lower resource competition of larger phytoplankton and increased grazing resistance against smaller grazers has often been used in ecological models to allow bloom formation of large phytoplankton (Kretzschmar et al. 1993; Ingrid et al. 1996; Leibold 1996; Terseleer et al. 2014). Chlorophyll concentration in the ocean, therefore, results from interlinking environmental conditions, plankton community size-structure and food webs.

Chlorophyll observations often serve to constrain large-scale biogeochemical models used to elucidate the dynamics of marine ecosystems and productivity across trophic levels, and project ecosystem changes that might result from global environmental change. These models, however, generally fail to capture the entirety of observed chlorophyll range and frequency distribution (Figure 1A) (Hashioka et al. 2013). Global biogeochemical models are adept at reproducing the very low chlorophyll observed in the oligotrophic regions but are often not able

to match much higher values (3-10 mg chlorophyll m^{-3}) in intensely productive coastal regions,
122 or vice versa. This shortcoming is apparent when comparing the range of chlorophyll concentration from remote sensing observations with the output of a selection of models used in
124 the fifth Coupled Model Intercomparison Project (CMIP5) (Figure 1A). Even regional models covering areas of broad ecological gradients, such as the California Current System (CCS),
126 apparently lack the ability to simulate the frequency distribution and/or the full range of very low surface chlorophyll concentrations offshore to high coastal chlorophyll concentrations observed
128 *in situ* (Figure 1B) (Gruber et al. 2006; Goebel et al. 2010; Gruber et al. 2011; Chenillat et al. 2013; Guo et al. 2014; Chenillat et al. 2015; Renault et al. 2016).
130

It has been hypothesized that the lack of very high chlorophyll conditions in most global
132 earth system simulations arises primarily from under-representation of the intense circulation and mixing processes in coastal regions that often feature the highest chlorophyll values (Stock et al.
134 2011), even in highly size-structured models (Ward et al. 2012). This is particularly true for eastern boundary upwelling systems where global models exhibit some of their largest biases.
136 However, prototype high-resolution earth system simulations, featuring 1/10° horizontal ocean resolution (Stock et al. 2017), and some eddy resolving regional simulations with ~5-15 km
138 horizontal resolution (Gruber et al. 2006; Goebel et al. 2010; Gruber et al. 2011; Chenillat et al. 2013; Guo et al. 2014; Chenillat et al. 2015; Renault et al. 2016) are also challenged in
140 representing the full observed chlorophyll dynamical range or its spatial distribution. While submesoscale dynamics requiring ~1 km resolution (e.g., fronts) can also facilitate
142 phytoplankton blooms and associated export production by injecting nutrients into surface waters (Omand et al. 2015; Stukel et al. 2017), simulations to date suggest that refined spatial resolution
144 alone may not be sufficient to capture high coastal chlorophyll.

146 In this study, our goal is to test whether improved resolution of the phytoplankton-grazer interactions can enable models to capture the dynamic range of chlorophyll concentration across
148 an ecological gradient from productive to oligotrophic ecosystems, representative of the global oceans. The well-studied CCS, which features intensely productive and oligotrophic regions in
150 close proximity, is used as a test region. We hypothesize that simulating the observed range of chlorophyll requires both high spatial resolution of circulation and improved representation of

the ‘sequential invasion’ and ‘grazer decoupling’ mechanisms described above. A planktonic ecosystem model with a canonical two size-class phytoplankton structure, the Carbon, Ocean Biogeochemistry and Lower Trophics (COBALT) model (Stock et al. 2014), is amended to include an additional large coastal diatom group to test this hypothesis. Briefly, the new coastal diatom group has a larger individual cell size than the current large phytoplankton group in the COBALT model and implicit chain-forming is assumed to further protect it from grazing by smaller zooplankton groups. Furthermore, rapid diatom growth rates relative to similarly sized phytoplankton from other taxonomic groups (Edwards et al. 2012 their Figure 3) minimizes allometric penalties associated with large size, increasing the potential for trophic decoupling. After assessing the ability of our coastal diatom addition to improve the range of chlorophyll concentration, we explore implications for the simulation of coastal hypoxia.

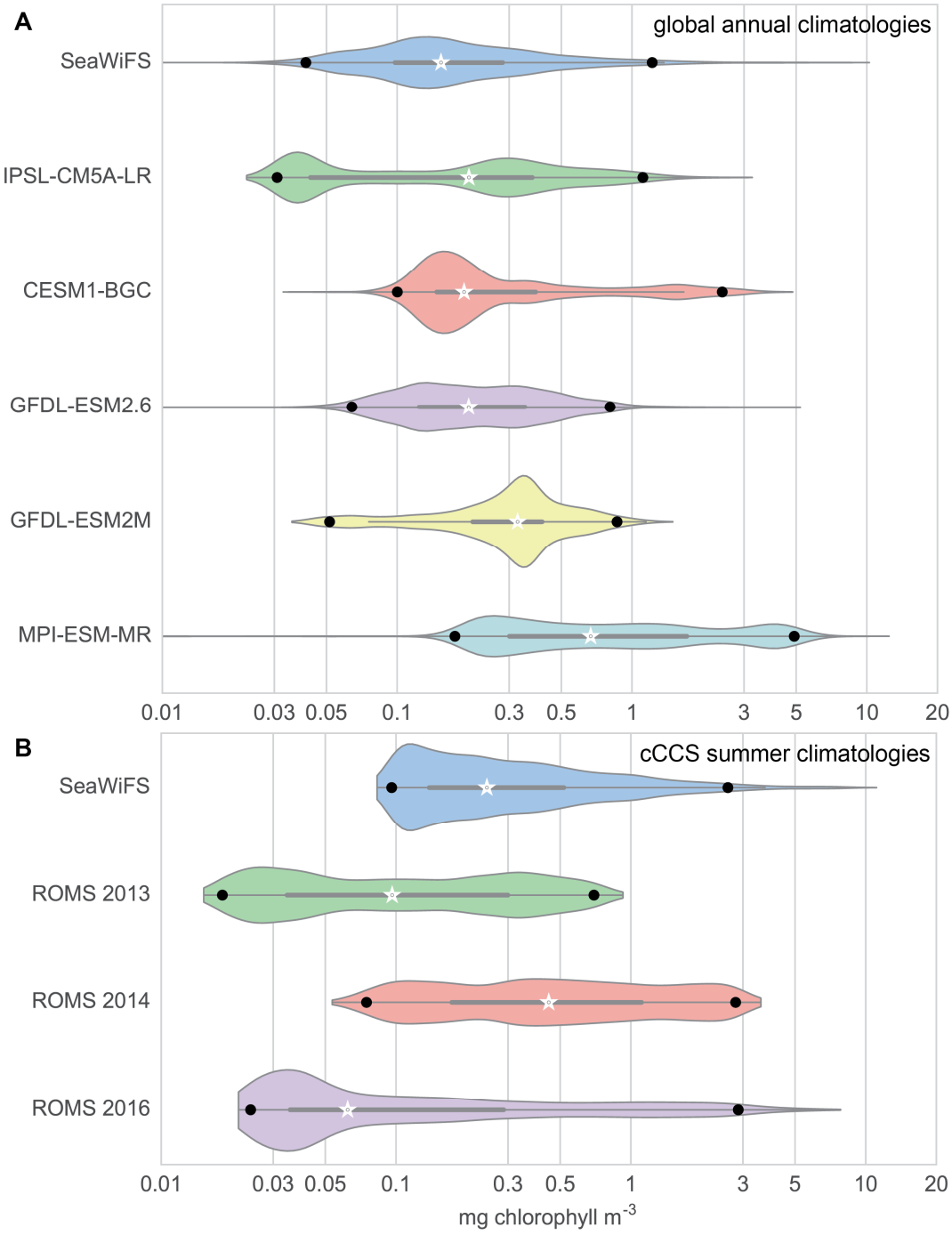

Figure 1. Comparison of marine chlorophyll concentration range and distribution from remote sensing observations (SeaWiFS) and (A) global CMIP5 models and (B) regional CCS models output. The violin plots show the median (white star), interquartile range (thickened gray line) and the 2.5 and 97.5 percentiles (black dots) overlaid onto the kernel density estimation of the (A) global, annual climatology or (B) central CCS, summer climatology of chlorophyll

concentration. Note that only the global IPSL model can match the large 2.5 to 97.5 percentile range (~0.04 - 1.22 mg chlorophyll m^{-3}) from SeaWiFS data (but not its distribution), with models capturing the low end of the range falling short at the high end and vice versa. Only ROMS 2014 and 2016 captures the 2.5 to 97.5 percentile range (~0.10 - 2.59 mg chlorophyll m^{-3}) from regional SeaWiFS data, however more than half of data points fall below the observed range in ROMS 2016 and ROMS 2014 does not simulate concentrations >4 mg chlorophyll m^{-3}. SeaWiFS data was provided at 1/12° and (A) regridded to 1° resolution for the global comparison. Global model data were regridded to 1° resolution and their latudinal coverage was limited to that of monthly SeaWiFS data. Seasonal climatological chlorophyll data from CMIP5 model runs were retrieved from the climate change web portal at the Earth System Research Laboratory (Scott et al. 2016), http://www.esrl.noaa.gov/psd/ipcc/ocn/, and used to compute the annual climatology. Model acronyms and their marine biogeochemical component: IPSL is the Institut Pierre Simon Laplace model (Dufresne et al. 2013) using the Pelagic Interaction Scheme for Carbon and Ecosystem Studies (PISCES) (Aumont and Bopp 2006), CESM is the Community Earth System Model (Hurrell et al. 2013; Lindsay et al. 2014) using the Biogeochemical Elemental Cycling (BEC) model (Moore et al. 2001), GFDL-ESM2M is the Geophysical Fluid Dynamics Laboratory model (Dunne et al. 2012) using the Tracers of Ocean Phytoplankton with Allometric Zooplankton code version 2.0 (TOPAZ2) (Dunne et al. 2013), GFDL-ESM2.6 is the high resolution Geophysical Fluid Dynamics Laboratory model using COBALT (Stock et al. 2017), MPI is the Max Planck Institute for Meteorology Earth System Model (Giorgetta et al. 2013) using the Hamburg ocean carbon cycle model (HAMOCC) (Ilyina et al. 2013). Central CCS chlorophyll concentration data from regional models ROMS 2013 with ~15 km (Chenillat et al. 2013), ROMS 2014 with ~14 km (Guo et al. 2014) and ROMS 2016 with ~5 km horizontal resolution (Renault et al. 2016), obtained through personal communication with the authors.

196 # 3 Methods

3.1 Model study domain, physical forcing and configuration

198 The full study domain spans the zonal extent of the CCS, from Vancouver Island (50°N) to southern Baja California Peninsula (20°N), extending up to 1200 km offshore parallel to the
200 coast. This study focuses on the central part of the CCS as a quintessential example of the CCS coastal upwelling system with a narrow continental shelf and a sharp offshore to near-shore
202 ecosystem gradient, spanning chlorophyll concentrations from ~0.03 to >10 mg m^{-3} over an average summer (upwelling favorable) season. The central CCS subdomain extends from Point
204 Conception in the south to Cape Mendocino in the north along the coast to 600 km from the shore, comprising the coastal, transition and offshore oligotrophic zones. The coastal region of
206 the central CCS was operationally defined as the subdomain extending from the shore to 100 km offshore, approximately corresponding to the 1 mg chlorophyll m^{-3} contour. Our analysis spans
208 the years 1996-2006, overlapping with the years of Sea-viewing Wide Field-of-view Sensor (SeaWiFS) chlorophyll data availability. Because this study aims to improve the representation
210 of the entire concentration range of marine chlorophyll, our analysis is centered on the summer months June, July and August (JJA), halfway into the coastal upwelling season in the central part
212 of the CCS, when coastal chlorophyll concentration is still high following upwelling events and offshore chlorophyll concentration is low due to surface nutrient depletion.

214

The CCS domain was simulated using a version of the Regional Ocean Modeling System
216 (ROMS) from Rutgers University (Curchitser et al. 2005; Shchepetkin and McWilliams 2005; Powell et al. 2006; Hermann et al. 2009) at 1/15° or ~7 km horizontal resolution. The model uses
218 the default third order upstream scheme for advection of momentum and the fourth order centered horizontal advection scheme for all tracers. Mixing of momentum and tracers is
220 performed along terrain-following surfaces (n=50) and geopotentials on a stretched vertical grid. The diffusion of momentum and tracers uses a Laplacian scheme with a viscosity of 25 $m^2 s^{-1}$
222 and diffusivity of 5 $m^2 s^{-1}$, and a quadratic bottom friction with a drag coefficient of $3 \cdot 10^{-3}$. Tides were excluded since their inclusion did not bring improvements to the simulation and their
224 exclusion allowed for a substantial increase in computational speed. Solar radiation is applied with an diurnal cycle, and sea surface salinity is restored to the monthly climatology from World

Ocean Atlas 2013 (WOA13) (Garcia et al. 2013) with a 90-day timescale. The light penetration depth depends on the chlorophyll concentration, using the formulation of (Manizza et al. 2005). Air-sea fluxes are computed using Coordinated Ocean-ice Reference Experiment (CORE) bulk formulae (Large and Yeager 2004).

Boundary and initial conditions for ocean dynamics, such as temperature, salinity, and velocity, are provided by the Simple Ocean Data Assimilation (SODA) model output v2p1p6 (Carton and Giese 2008) and atmospheric forcing is provided by the Modern Era Retrospective-analysis for Research and Applications (MERRA) atmospheric reanalysis product. Macronutrients and oxygen concentrations are initialized with WOA13 (Garcia et al. 2013), forcing for dissolved inorganic carbon and alkalinity is based on Global Ocean Data Analysis Project (GLODAP) data (Key et al. 2004). Values of the remaining COBALT variables were initialized from a global retrospective simulation (Stock et al. 2014). Iron deposition is based on dust deposition of Moxim et al., (2011) with iron content and solubility from Fan et al., (2006). Iron sources from the sediment are based on Elrod et al., (2004) with an additional coastal source of similar magnitude to that of the sediment. The atmospheric CO_2 concentration is provided by the monthly mean global CO_2 estimates from NOAA/ESRL (www.esrl.noaa.gov/gmd/ccgg/trends/), which were linearly interpolated in time. River and coastal runoff data originate from the dataset in Dai et al. (2002), which were remapped conservatively onto the regional domain and added as a freshwater source to the surface layer. Coastal nutrient input by rivers was driven by the product of nutrient concentration from the global NEWS climatology (Seitzinger et al. 2005) and the river and coastal runoff water flux from Dai et al. (2002).

3.2 Observational datasets

Several observational datasets were used to assess the ability of the model simulations to reproduce the temporal, spatial and statistical distribution of chlorophyll, relative phytoplankton size class abundance, mesozooplankton biomass and near-bottom dissolved oxygen levels. The model's sea surface temperature (SST) fidelity with observed cross-shore SST gradients was assessed against optimal interpolated SST data from NOAA's National Centers for Environmental Information (NOAA IO.v2) (Reynolds et al. 2007),

https://www.ncdc.noaa.gov/oisst. Upwelling was assessed against monthly upwelling indices from 1996-2006 provided by NOAA Pacific Fisheries Environmental Laboratory (PFEL), https://www.pfeg.noaa.gov/products/PFEL/modeled/indices/upwelling/NA/data_download.html. The cross-shore depth distributions of chlorophyll, nitrate, temperature and potential density were assessed using summer climatological means along CalCOFI line 67 (from 1997-2013, starting near Monterey bay at 36.8°N 121.9°W and extending southwest, perpendicular to the coast to 34.5°N 127°W; https://www3.mbari.org/bog/data/Line67_BCTD.csv). These data were collected by Francisco Chavez and the Biological Oceanography Group at Monterey Bay Aquarium Institute (MBARI).

Surface chlorophyll was estimated from the SeaWiFS remote sensing data, using the 2014 processing version. More specifically, we used monthly climatological composites (level 3) obtained from the Distributed Active Archive Center at NASA Goddard Space Flight Center (SeaWiFS Level-3 Mapped Chlorophyll Data Version 2014). Remote sensing products are prone to overestimating chlorophyll concentration in coastal areas due to the presence of colored dissolved organic matter (Schofield et al. 2004). Match-ups between remotely sensed chlorophyll and in situ chlorophyll concentration measurements in the California Current System, however, indicate that chlorophyll concentrations up to 47 mg m^{-3} are not overestimated by remote sensing products (Kahru et al. 2014). There was in fact a modest negative bias of remotely sensed chlorophyll at concentrations >1 mg m^{-3}, thus underestimating medium to high in situ chlorophyll concentrations in the California Current System.

The SeaWiFS chlorophyll values were bilinearly interpolated onto the ROMS model domain grid to allow co-localized comparison between observations and model results. Since 90% of water-leaving radiance signal detected by remote sensing originates from the first optical depth, simulated chlorophyll concentrations were averaged over this depth layer. The first optical depth has been operationally defined as the depth where short wave radiation had been attenuated to e^{-1} or ~37% of its surface intensity (Gordon and McCluney 1975), and typically varied between 5 and 15 m in the model simulations based on modelled short wave light attenuation.

Size-partitioned fractional chlorophyll distribution was estimated from three different satellite-based algorithms using calibrated relationships between size class-specific marker pigments and total chlorophyll concentration according to Hirata et al. (2011) and absorption spectra (Roy et al. 2013). The relative concentrations of pico- to micro-sized organic carbon particles (POC) were derived from the spectral slope of particulate backscattering coefficients according to Kostadinov et al. (2009; 2016). The COBALT model's diazotroph phytoplankton group was not included in the size-partitioned analyses because of its low contribution to total primary production, 1.4±0.7% in top 100 m of central CCS, and their equivocal affiliation to either pico- or micro-sized functional groups from remote sensing-based algorithms.

Monthly mesozooplankton carbon biomass measurements were retrieved from NOAA's Coastal & Oceanic Plankton Ecology, Production & Observation Database (COPEPOD) (http://www.st.nmfs.noaa.gov/copepod/2012/biomass-fields.html), a global plankton database project of the US National Marine Fisheries Service (Moriarty and O'Brien 2013). Briefly, estimates of mesozooplankton biomass include data from net tows, with mesh size 200-505 µm, over the top 200 m of the water column, going back to the 1950's. These data were converted to a common biomass unit in their equivalent 333 µm mesh size values (µg C l^{-1}), regridded to a 0.25°, and averaged over the top 200 m and seasonally.

Near-bottom oxygen measurements along the US West coast continental shelf and slope (2009-2015, 32.06 - 48.44°N, <1250 m depth), as described in Keller et al. (2015), were provided by NOAA's Northwest Fisheries Science Center (https://www.nwfsc.noaa.gov/data). To define hypoxia, i.e. dissolved-oxygen deficit, we use the concentration threshold of 1.43 ml l^{-1} (equivalent to 63.87 µmol l^{-1}) commonly used in benthic ecological studies (Keller et al. 2015).

3.3 Ecosystem model configuration

We use the COBALT marine ecosystem model as our baseline model control, which was implemented into the ROMS model. Before describing the amendments we have made to the baseline model, we provide an abbreviated description of the model elements required to understand the trade-offs between functional groups pertinent to the experiments herein.

318 Complete details of the model's governing equations and parameter values be found in Stock et al. (2014).

320

COBALT's baseline plankton food web structure (Figure 2A) is similar to other planktonic food
322 web models coupled with ocean simulations at global and regional scales, e.g., PISCES (Aumont and Bopp 2006), CoSiNE (Chai et al. 2002), NEMURO (Kishi et al. 2007). COBALT is in
324 essence a box model and the parameters used to represent the physiological and trophic size dependence are informed by allometric constraints. Phytoplankton groups fall into two size
326 classes, a small and a large one, to capture contrasts between food webs with highly efficient nutrient recycling, dominated by small plankton, and more export-prone large phytoplankton-
328 dominated food webs (Tremblay et al. 1997). While the nominal division between small and large phytoplankton in the baseline model is an equivalent spherical diameter (ESD) of ~10 µm,
330 as with most plankton functional type models, considerations of particle size inform the model but the formulation does not strictly follow allometric scaling rules. The primary competitive
332 advantage of small phytoplankton over larger phytoplankton is more effective nutrient and light uptake at low ambient nutrient concentrations and light levels (Munk and Riley 1952; Edwards et
334 al. 2012; 2015), while the primary advantage of large phytoplankton is that they escape predation by microzooplankton due to their larger prey-to-predator size ratio (Hansen et al. 1994; 1997).
336 These trade-offs allows the baseline model to successfully capture observed shifts in the relative prevalence of small versus larger phytoplankton across ocean biomes (Stock et al. 2014).

338

Three zooplankton size classes consume the phytoplankton groups and smaller zooplankton size
340 classes. These are parameterized as microzooplankton, small to medium-bodied copepods, and large copepods and krill, in order of increasing size class. Maximum biomass-specific grazing
342 rates decrease from small to large following Hansen et al. (1997), with common half-saturation constants calibrated to reproduce observed prey biomass and turnover rates across ocean biomes
344 (Stock and Dunne 2010). Zooplankton feeding is modeled with a Type II Holling functional response for a single prey type with weak biomass-based prey switching between alternative
346 prey types as described in Stock et al. (2008). Phytoplankton are also subject to aggregation through a simple density dependent loss term (Doney et al. 1996) calibrated based on Jackson et

al. (2001; 1990). The aggregation response, which leads to sinking loss is suppressed when nutrients and light are not strongly limiting (Waite et al. 1992b; a).

Two aspects of the baseline COBALT formulation are notable with respect to the sequential invasion and trophic decoupling mechanisms proposed to control chlorophyll concentrations along a productivity gradient (see Introduction). First, there are only two size classes that can invade (Figure 2A). When resources reach a minimal level to allow a population to be sustained relative to metabolic costs small phytoplankton have a competitive advantage. Large phytoplankton invade at higher resource levels and once small phytoplankton are controlled by microzooplankton. Second, the one large phytoplankton group is subject to top-down control by medium and large zooplankton (i.e., small copepods to krill). While these groups have lower biomass-specific grazing rates than microzooplankton (Hansen et al. 1997), they span equivalent spherical diameters from ~0.2-20 mm. This limits the potential for transient consumer-prey temporal decoupling and thus biomass accumulation, i.e., blooms. Thus, while two size classes were sufficient for capturing first-order shifts in recycling versus export-prone food webs across ocean biomes, this coarse resolution of phytoplankton communities appears to fall short in intensely productive near-shore regions.

We test the hypothesis that a third phytoplankton size class with a distinct predator-prey link can address this limitation. Modifications to the baseline COBALT model for our experiments pertain primarily to the growth parameterization and predator-prey links in the amended model. The new, amended 3PS-COBALT model includes three zooplankton and three phytoplankton size classes (Figure 2B). Small phytoplankton (P^S) remain those consumed by microzooplankton. A new 'medium' size class (P^M) designates the nanophytoplankton group that is readily consumed by small copepods, and a new '3PS-large' size class (P^{3L}) represents the microphytoplankton group, parameterized as larger, chain-forming phytoplankton such as diatoms, grazed only by large copepods and krill (Slaughter et al. 2006; Stukel and Ohman 2013; Taylor et al. 2015). The model structure and trophic relationships (Figure 2B) are similar in the larger groups to the early allometric models of Moloney and Field (1991), and allow for both an additional sequential invasion (i.e., another distinct phytoplankton-zooplankton coupling) and the possibility of greater trophic decoupling (i.e., large phytoplankton are controlled only by large

zooplankton). The structure in Figure 2B remains, as in all plankton models, greatly simplified relative to the full scope of possible plankton interactions. However, it reflects an improved, yet still computationally efficient, depiction of primary plankton food web links in Figure 2A with the specific objective of improving representation of the observed chlorophyll range (Figure 1). We discuss potential impacts of remaining structural simplifications, and the relationships between our results and those derived from highly resolved size-based or emergent diversity plankton models in the Discussion.

In the amended 3PS-COBALT model, parameter values were chosen to represent a more refined version of the trade-offs present in the baseline COBALT model, having two phytoplankton size classes. Parameter values for the new phytoplankton groups are presented in Table 1. The remaining parameter values for the medium and 3PS-large groups are the same as those for the large phytoplankton group in Stock et al. (2014). Half-saturation constants for nutrient uptake (K) increase from small to large phytoplankton size classes (Edwards et al. 2012), following allometric principles suggesting that the larger surface area to volume ratio of small cells is conducive to more effective scavenging for nutrients in low nutrient environments (Munk and Riley 1952; Aksnes and Egge 1991). Iron limitation is modeled with a cell quota model, where the scaling of the half-saturation constant Fe:N ratio to growth is based on values reported in Sunda et al. (1995; 1997). Unlike K, the maximum carbon-specific photosynthesis rate (P_{Cmax}, d^{-1}) is relatively constant for the three phytoplankton size classes. This choice is motivated by two observations: a) phytoplankton maximum growth rates peaks among cells ~6 µm in diameter and declines for larger and smaller cells (Marañón et al. 2013), and b) diatoms as a group have higher maximum growth rates relative to other, similarly sized groups (Banse 1982; Tang 1995; Sarthou et al. 2005; Edwards et al. 2012). These two factors suggest that rather small differences in P_{Cmax} for our model phytoplankton size classe can be justified, despite the known allometric scaling for maximum growth rate. The unimodal size dependence of maximum growth rates is thought to result from constraints on the rate of nutrient uptake at the smallest cell sizes (Raven 1998; Marañón et al. 2013; Ward et al. 2017) and from constraints on the distribution of resources within cells for larger cell sizes (West 1997; Brown et al. 2004). Smaller phytoplankton have a steeper initial slope of the chlorophyll-specific photosynthesis-light relationship (α) due to a smaller chlorophyll packaging effect (Morel and Bricaud 1981), but a lower maximum

chlorophyll to carbon ratio (θ_{max}) (Geider 1993). Large phytoplankton are subject to stronger losses via aggregation based on model analyses by Jackson et al. (2001; 1990).

We chose parameter values meeting these empirical constraints (Table 1), but also tested a range of values for the model within a ~140 x 35 km near-shore to offshore subset of the CCS model domain (see Supp. Figure 6 and Supp. Text). These experiments emphasized the importance of parameterizing the 3PS-large phytoplankton group in a manner consistent with chain-forming diatoms with individual cell sizes between ~20-50 µm ESD in order to capture the prominence of this group in upwelling systems (Venrick 2009; Taylor et al. 2015). This choice allows for only modest nutrient uptake and maximum growth rate penalties relative to the medium phytoplankton (Table 1), while implicit spine-bearing and chain formation is presumed to create prey sizes large enough to deter smaller grazers (Smetacek 1999; Slaughter et al. 2006).

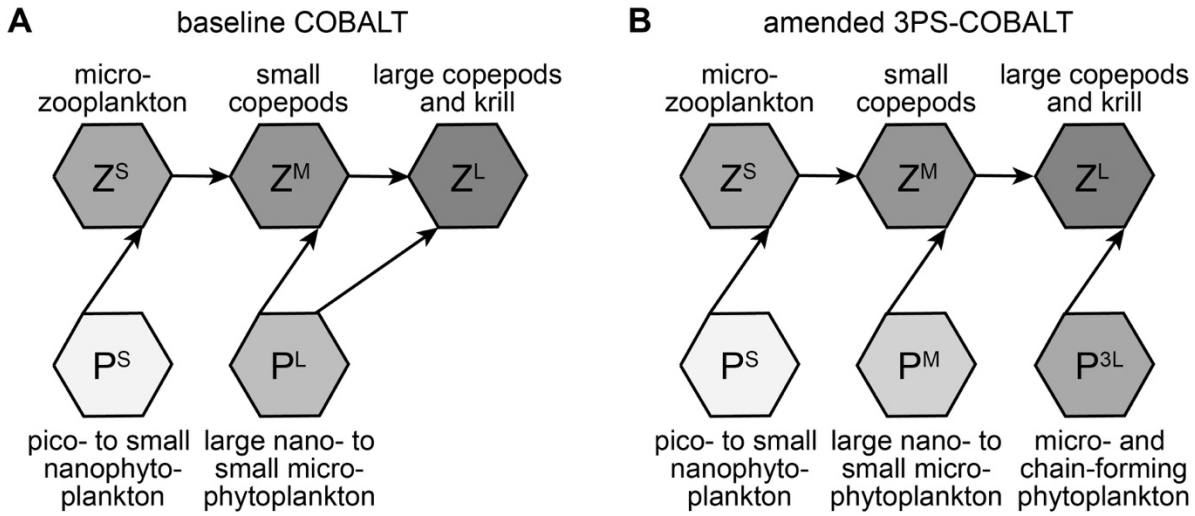

Figure 2. Depiction of the trophic relationships between the different phytoplankton (P) and zooplankton (Z) size classes in the (A) baseline COBALT and (B) amended 3PS-COBALT model configuration, which resolves three phytoplankton size classes.

parameter	P^S	P^M	P^L	units	ref.
P^C_{max} @0°C	1.125	1.250	1.125	d^{-1}	1, 2, 3, 4
K_{NO3}	0.50	1.50	2.25	mmol m^{-3}	5, 6
K_{NH4}	0.10	0.30	0.45	mmol m^{-3}	7, 8
K_{PO4}	1.0×10^{-2}	3.0×10^{-2}	4.5×10^{-2}	mmol m^{-3}	9
K_{SiOH4}	na	1.00	1.50	mmol m^{-3}	10, 11
K_{Fed}	1.0×10^{-4}	3.0×10^{-4}	4.5×10^{-4}	mmol m^{-3}	11
K_{FetoN}	1.99×10^{-5}	2.39×10^{-5}	3.58×10^{-5}	mol Fe mol^{-1} N	12, 13
α	2.0×10^{-5}	1.3×10^{-5}	1.2×10^{-5}	g C g^{-1} chl m^2 μmol^{-1} γ	14, 15
θ_{max}	0.03	0.05	0.07	g chl g^{-1} C	14, 15
aggregation	$1\times10^{+5}$	$3\times10^{+5}$	$6\times10^{+5}$	d^{-1} mol^{-1} N kg^{-1}	16, 17
	ZS	**ZM**	**ZL**		
$ingest_{max}$ @0°C	1.42	0.57	0.23	d^{-1}	18, 19
K_{ingest}	1.25×10^{-6}	1.25×10^{-6}	1.25×10^{-6}	mol N kg^{-1}	18, 19

Table 1. Parameter values of primary physiological trade-offs for each phytoplankton and zooplankton size class used in the amended 3PS-COBALT model. Note that P^L parametrization choices were made to capture the characteristics of chain-forming coastal diatoms common in upwelling and spring bloom conditions. The *K* parameters are half-saturation constants for nutrient limited growth (see Stock et al. (2014) for details). Other abbreviations are as given in the main text, chlorophyll (chl). Literature references (ref.) upon which the parameter values are based: (1) Bissinger et al. (2008), (2) Banse (Banse 1982), (3) Tang (1995), (4) Marañon et al. (2013), (5) Eppley et al. (1969), (6) Romeo and Fisher (1982), (7) Eppley and Renger (1974), (8) Frost and Franzen (1992), (9) Lomas et al. (2014), (10) Martin-Jézéquel et al. (2000), (11) Sarthou et al. (2005), (12) Sunda and Huntsman (1997), (13) Sunda and Huntsman (1995), (14) Geider (1993), (15) Geider et al. (1997), (16) Jackson (1990), (17) Jackson (2001), (18) Hansen et al. (1997), (19) Stock and Dunne (2010). Model parameter values not listed here are as in Stock et al. (2014).

3.4 Skill assessment of model simulations

Several skill metrics are used to quantify model-observational data fits: Pearson's correlation coefficient (r) is used as a measure of relative spatial agreement; the mean difference between model and observations (bias) and the root mean square error (RMSE) are used to quantify the scale of the difference between the model and data for any given point; and for chlorophyll concentration, the median and the 2.5 and 97.5 percentiles is used as an additional measure of model-data comparison focusing on the range and distribution of the data (see results in Supp. Tables 1 and 2). Chlorophyll concentration were $\log_{10}$-transformed prior to skill assessment and the arithmetic mean of untransformed data is provided ± one standard deviation. In order to simplify comparison between observations and simulations, the figure panels are arranged in the following sequence: baseline COBALT model results, observational data, amended 3PS-COBALT model results.

4 Results

4.1 Seasonal occurrence of coastal upwelling and phytoplankton blooms

Coastal upwelling intensity typically peaks in early summer along the central CCS (Figure 3, shaded areas) when cold deeper water surfaces near the coast. Both models are able to reproduce this seasonal upwelling cycle, as approximated by the decline in coastal SST relative the offshore SST with increasing upwelling intensity (Figure 3, dashed lines). The larger amplitude in simulated SST gradient is due to the warm offshore temperature bias in the model (Supp. Figures 1 and 2). Coastal upwelling triggers phytoplankton bloom formation resulting in chlorophyll accumulation (Figure 3, blue line). Both models succeed in simulating a chlorophyll accumulation as a response to increased upwelling, yet only the amended 3PS-COBALT model matches the in situ observations in both amplitude and timing (Figure 3, red line; in situ chlorophyll concentration vs. baseline COBALT : r=0.31, p=0.27, mean bias=-2.17 mean RMSE=2.59 ; in situ chlorophyll concentration vs. 3PS-COBALT: r=0.61, p<0.05, mean bias=-0.76 mean RMSE=1.42).

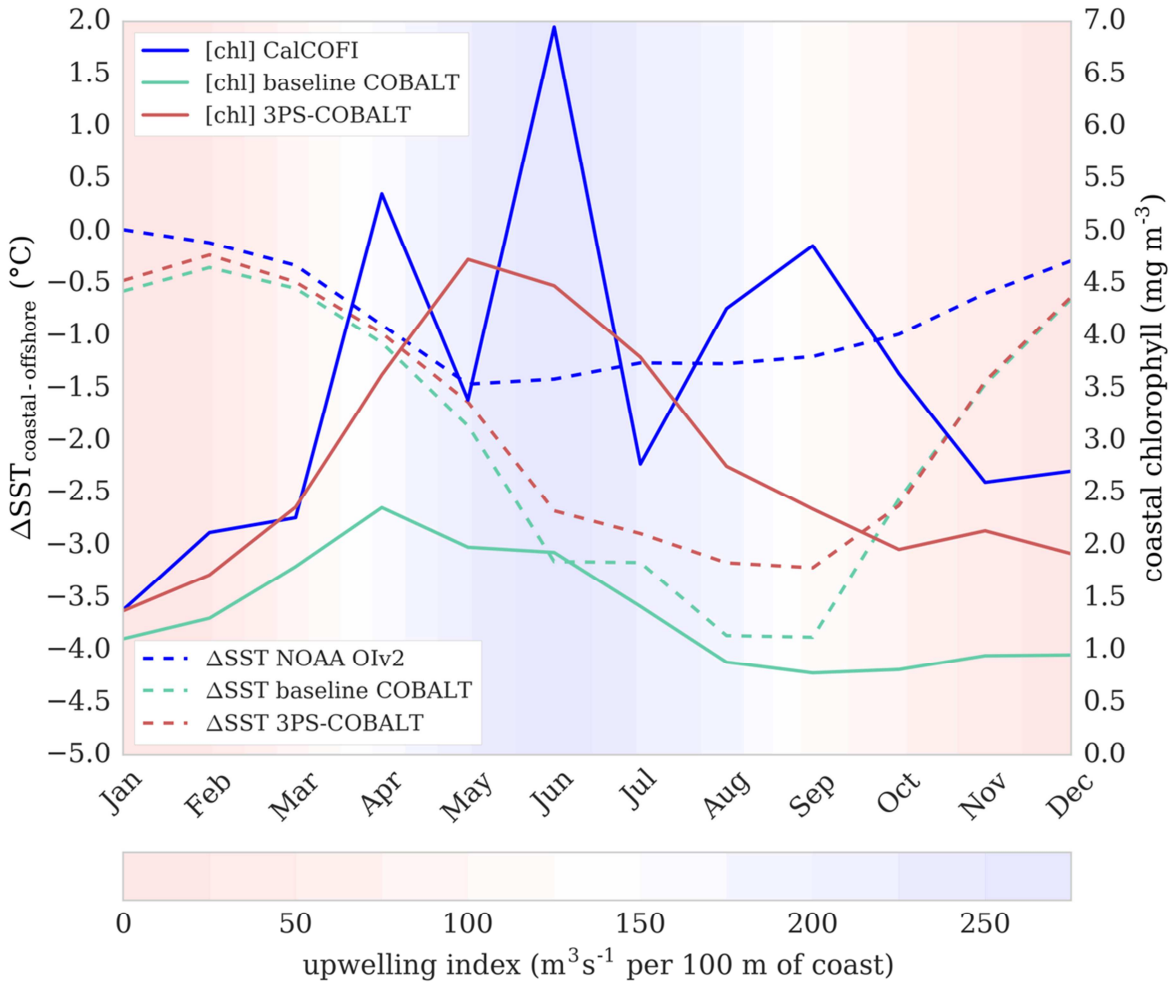

Figure 3. Monthly climatologies of upwelling index, chlorophyll concentration in the coastal area and sea surface temperature difference between coastal and offshore areas in the central CCS. Maximum upwelling index from NOAA PFEL at 36°N (color shading) corresponds to peak in situ chlorophyll concentration from CalCOFI line 67 (blue line) (0-10 m, 121.84-122.25°W 36.72 °N, 1997-2013) and a larger difference in the sea surface temperature (NOAA OI.v2) between coastal and offshore area, characteristic of upwelling season progression (dashed blue line). The seasonal coastal upwelling cycle is simulated by both model configurations (green and red lines), yet only the amended 3PS-COBALT model reproduces the timing and amplitude of the observed seasonal change in chlorophyll concentration (red line). In situ chlorophyll data collected by Francisco Chavez and the Biological Oceanography Group at MBARI.

4.2 Chlorophyll concentration range and distribution along a productivity gradient

Observed SeaWiFS summer chlorophyll concentration in the CCS spanned more than three orders of magnitude from ~0.05 mg m^{-3} at the offshore boundary of the ROMS model domain to >10 mg m^{-3} nearshore (Figure 4A), with a sharp chlorophyll gradient dropping to <1 mg m^{-3} approximately 100 km from shore (Figure 4A inset). The 2 phytoplankton size class baseline simulation (Figure 4B) captures the very low offshore chlorophyll concentration, but peak chlorophyll in coastal regions reach only ~2 mg m^{-3}, despite improved spatial resolution achieved by the ROMS model relative to global simulations (for detailed statistics on chlorophyll concentration comparisons see Supp. Table 1). This is consistent with the magnitude of peak chlorophyll values found in high-resolution (~10 km) global simulations with baseline COBALT (Stock et al. 2017). The limited simulation of high coastal chlorophyll in the baseline model is further exemplified by the very narrow offshore extent of the 1 mg chlorophyll m^{-3} contour, which only extends ~100 km offshore in the small region between the Gulf of the Farallones and Monterey Bay in central CCS (Figure 4B inset).

The addition of the third phytoplankton size class, parameterized as a chain-forming diatom, allows the amended model to capture the very high chlorophyll concentration over the core of the coastal upwelling, where chlorophyll concentrations >1 mg m^{-3} extend up the 100 km offshore (Figure 4C inset) (Supp. Table 1). Concentrations of chlorophyll for both the remote sensing observations and the amended model routinely exceed 5 mg m^{-3} in the central CCS region, peaking at 9 mg chlorophyll m^{-3} in the simulated summer climatology. This is accomplished while maintaining chlorophyll concentration three orders of magnitude below these peak values at the offshore boundary of the central CCS (Figure 4C), in accordance with observations (Supp. Table 1). At the northern and southern ends of the domain chlorophyll concentration remains underestimated compared to remote sensing observations (Figure 4D). This is likely caused by insufficient nutrient input from circulation coming in from the north (Supp. Figure 3) and phytoplankton depleting coastal surface nutrients earlier than observed in the south (data not shown).

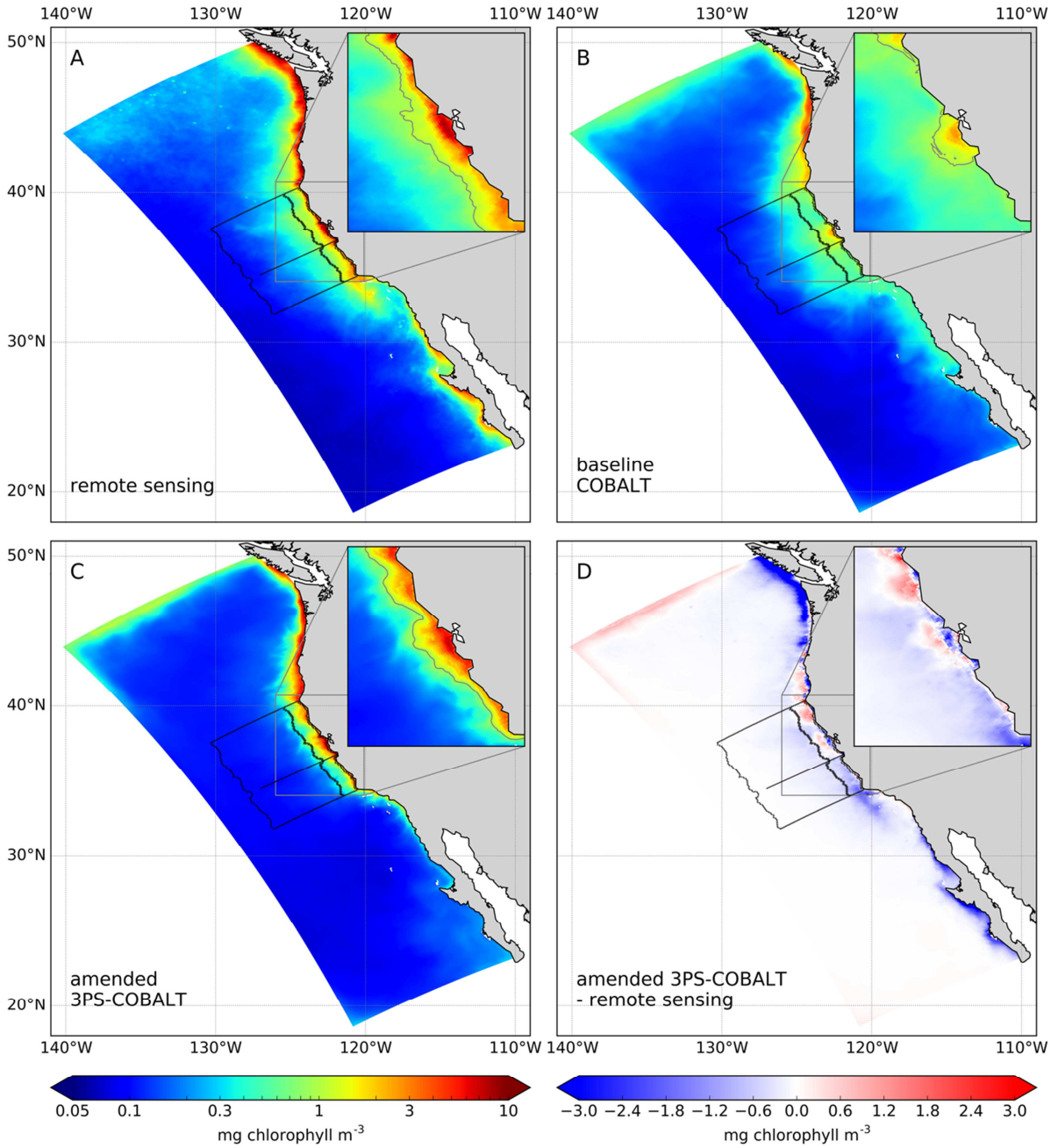

514 **Figure 4**. Summer climatology of chlorophyll concentration from (A) SeaWiFS observations, (B) 2 phytoplankton size class baseline COBALT model, and (C) 3 phytoplankton size class
516 amended 3PS-COBALT model. The difference in chlorophyll concentration between the 3PS-COBALT model and SeaWiFS observations is shown in panel D. The central CCS region,
518 between Point Conception and Cape Mendocino, is outlined in black from the shore to 100 km offshore (coastal region) and to 600 km offshore (coastal to offshore region). CalCOFI line 67 is

represented by the black cross-shore transect line. The inset details the chlorophyll in the coastal zone and the offshore extent of the 1 mg chlorophyll m^{-3} contour (gray contour line).

High chlorophyll concentrations (>5 mg m^{-3}) near the coast of Monterey Bay (36.8°N) are typical during summer upwelling season (Figures 4A and 5B). Further offshore, surface chlorophyll concentration decreases sharply and the chlorophyll maximum recedes deeper into the water column to 90-100 m, nearly following the 25.0 kg m^{-3} isopycnal (Figure 5B). While the baseline COBALT model reproduces the cross-shore decline in surface chlorophyll concentration, it lacks the ability to reproduce high coastal chlorophyll concentrations (<2 mg m^{-3}) and a distinct deep chlorophyll maximum further offshore (Figure 5A). The amended 3PS model on the other hand, reproduces both high coastal chlorophyll concentrations (>3 mg m^{-3}) and a distinct deep chlorophyll maximum further offshore, in agreement with observations, despite a more abrupt decline in surface chlorophyll concentration in the coastal to offshore transition zone (~122.5-123.5 °W).

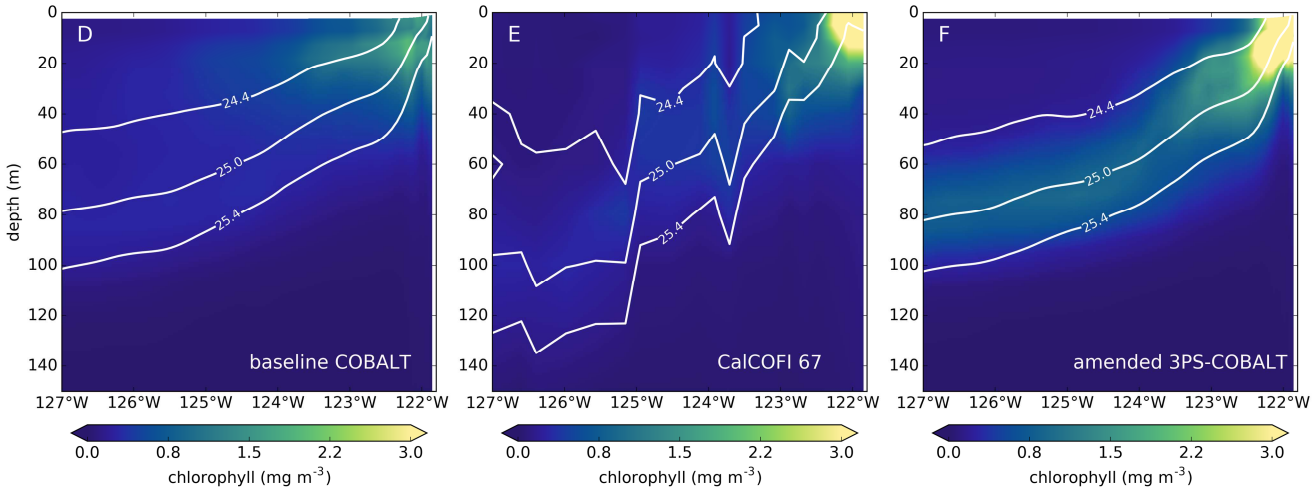

Figure 5. Cross-shore chlorophyll depth distribution along CalCOFI line 67 (black line in Figure 4) for (A) baseline COBALT model, (B) *in situ* chlorophyll measurements from CalCOFI and (C) amended 3PS-COBALT model. Isopycnals are overlaid in white (potential density, in kg m^{-3}). *In situ* chlorophyll and density data collected by Francisco Chavez and the Biological Oceanography Group at MBARI.

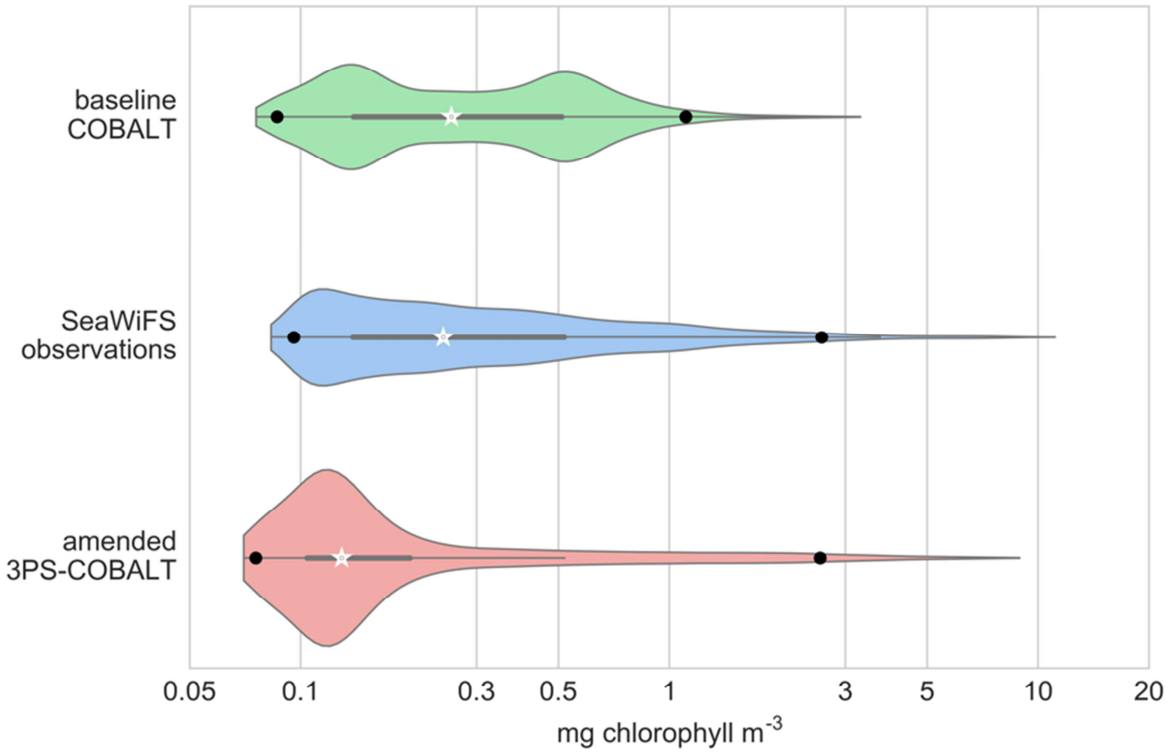

Figure 6. Comparison of chlorophyll concentration range and distribution from (top) 2 phytoplankton size class, baseline COBALT simulation, (middle) SeaWiFS remote sensing observations and (bottom) 3 phytoplankton size class, amended 3PS-COBALT simulation. The violin plots show median (white star), interquartile range (black bar) and the 2.5 and 97.5 percentile (black dots) overlaid onto the kernel density estimation of the chlorophyll concentration values of the months June, July, August in the central CCS region.

Comparison of the chlorophyll probability distributions in the central CCS (Figure 6) confirms that surface chlorophyll in the amended model formulation spans a similar range as the observations. The baseline model, in contrast, underestimates the high end of observed chlorophyll concentrations by a factor of ~2.5 at the 97.5 percentile level (Supp. Table 1). These results support the value of a third phytoplankton size class, parameterized as a chain-forming diatom, for capturing both high and low chlorophyll regions. However, the probability distributions also reveal either a surplus or a shortage of intermediate chlorophyll concentrations in the baseline or amended model, respectively, compared to remote sensing observations. This is also apparent in Figures 4 and 5 as either a too gradual cross-shore decline in chlorophyll

concentration for the baseline model or a more abrupt spatial decline from peak chlorophyll nearshore to reduced values offshore for the amended model compared to observations. The poor spatial representation of the chlorophyll concentration gradient in this coastal-to-offshore transition zone appears to be a common problem in CCS regional models (Goebel et al. 2010; Chenillat et al. 2013; Guo et al. 2014; Gruber et al. 2006).

Investigation of the origin of this misfit suggests that the more abrupt cross-shore transition may result from physical model biases. Most notably, despite generally good agreement in terms of spatial distribution of the SST (r =~1, p<0.001, CCS) (Supp. Figure 1), the ROMS model simulations exhibit a sharper cross-shore increase in water column stratification and warmer, more stratified overall off-shore conditions than observed (Supp. Figures 2 and 4). This is indicative of a more rapid cross-shore transition from upwelling to oligotrophic, highly stratified conditions in the model. Accounting for this bias by plotting surface chlorophyll concentration as a function of surface temperature (Supp. Figure 5) yields a decline of chlorophyll with increasing temperature that is consistent between the amended model simulation and observations. In the baseline model, however, chlorophyll levels of ~0.5 mg m^{-3} extend further offshore (Figure 4B and Figure 5B) because coastal phytoplankton production does not sufficiently consume surface nutrients (Supp. Figure 3), thus allowing the residual surface nutrients to be advected offshore despite the same overestimated thermal stratification. Despite outstanding issues in the resolution of the transition zone, significant improvements in the simulation of high coastal chlorophyll concentration (Figures 4, 5 and 6; Supp. Table 1) support further analysis of the impact of capturing these high chlorophyll regions on their biogeochemical ramifications, such as coastal hypoxia.

4.3 The impact of improved chlorophyll representation on simulated coastal bottom hypoxia

Strong gradients in near-bottom dissolved oxygen concentrations (DO), ranging from oxic to severely hypoxic, are observed in CCS shelf areas with bottom depths shallower than 150 m (DO in ml l^{-1}: 1.90 ±0.71, min=0.44, max=5.96, n=688) (Figures 7B and 8B). Only the amended model successfully reproduces the broad range of near-bottom DO on these shallow shelf areas (Figures 7C and 8C) (climatological summer mean of co-located DO in ml l^{-1}: 1.41±0.50, min=0,

590 max=2.65, n=202). The amended model also replicates the observed trend of decreasing near-bottom DO with increasing bottom depth along the CCS shelf areas (from 56 to ~600 m depth),
592 and the bottom depth (~360 m) where shelf areas are considered chronically hypoxic (i.e., DO <1.43 ml l^{-1}) during the months June, July and August (compare Figures 7B with 7C). Except for
594 the trend of decreasing near-bottom DO with increasing bottom depth, the baseline model could not reproduce levels of hypoxia in shallow shelf areas, nor the depth threshold below which most
596 CCS bottom waters become chronically hypoxic (climatological summer mean of co-located DO in ml l^{-1}: 2.41±0.31, min=1.94, max=3.44, n=202, ~500 m) and had a higher overall bias
598 compared to the amended model (compare Figures 7A and 8A with 7C and 8C). An improved representation of high coastal chlorophyll and phytoplankton size structure thus improved
600 simulated vertical patterns and levels of bottom hypoxia.

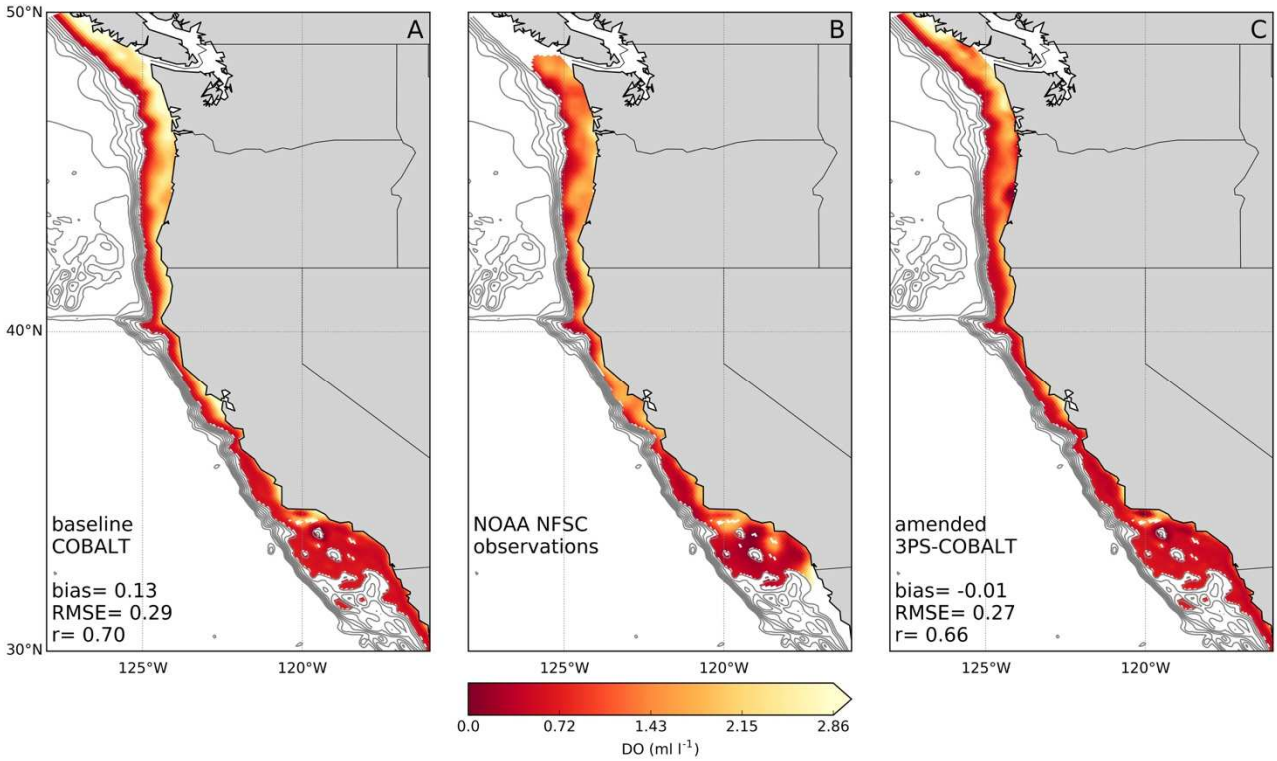

602

Figure 7. Spatial distribution of near-bottom dissolved oxygen (DO) concentration for bottom
604 depths shallower than 1250 m. (A) summer climatology simulated by the baseline COBALT model, (B) measured by NOAA Northwest Fisheries Science Center during trawling surveys
606 from 2009 to 2015 during the months June, July and August, and (C) summer climatology simulated by the amended 3PS-COBALT model. Bathymetric contour lines from 1250 to 3000

608 m depth with 250 m interval are shown to indicate the steepness of the continental slope. Note that simulations and observations of DO are well correlated (*r*) and that both simulations have a
610 similar accuracy as estimated by RMSE. The amended 3PS-COBALT model better simulates hypoxia levels on the shelf as indicated by the lower mean bias.
612

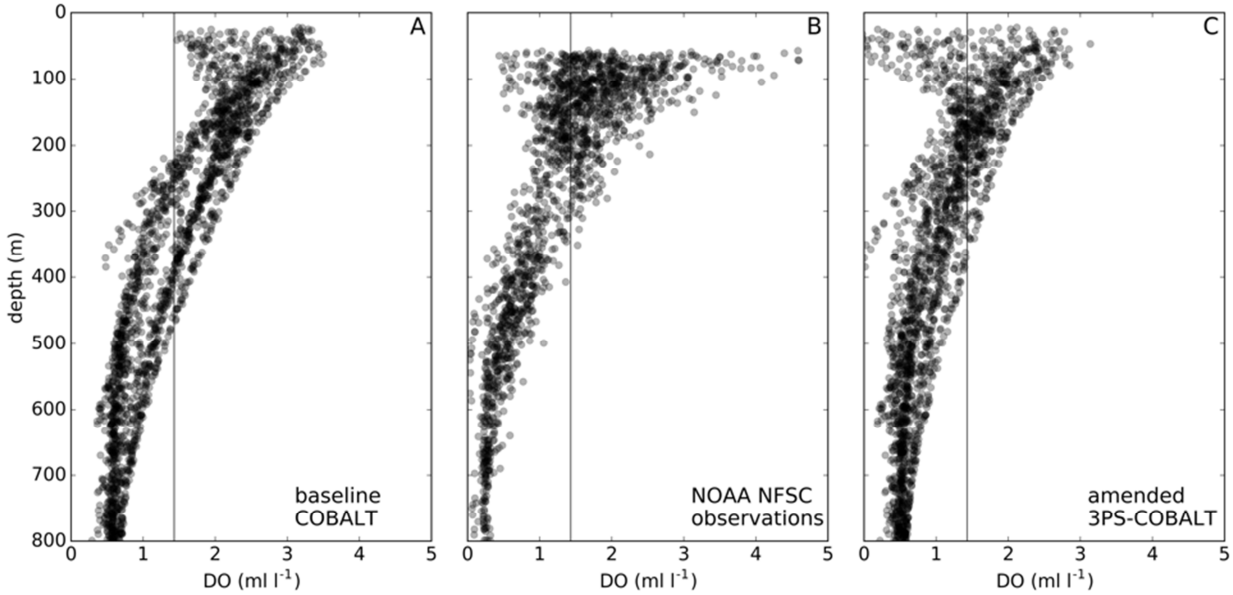

614 **Figure 8**. Near-bottom dissolved oxygen (DO) concentration on the California Current System continental shelf (32.06 - 48.44°N). (A) summer climatological means from the baseline
616 COBALT model simulation, (B) NOAA Northwest Fisheries Science Center measurements during the months June, July, and August between 2009 and 2015 (n=1765), (C) summer
618 climatological means from the amended 3PS-COBALT model simulation. Vertical line at DO = 1.43 ml l^{-1} denotes hypoxia threshold.
620

Oxygen consumption in near-bottom waters is fueled by microbial respiration of organic
622 matter exported from the photic zone. The bottom export flux of organic particulate matter in the coastal region of the central CCS was 0.54 mmol C m^{-2} d^{-1} in the amended model, i.e., ~2.6 times
624 higher than in the baseline model (Figure 9). The particle export ratio, i.e., the ratio of organic carbon to primary production flux at 100 m depth, from which the bottom flux derives, varied
626 around ~0.31±0.11 in the coastal region of the central CCS during summer. This is in the range of particle export ratios reported for the coastal region of the CCS, which can be as high as 0.4 to
628 0.5 (Wilkerson et al. 2000; Dunne et al. 2005, and references therein). The more intense organic

particulate export flux to the bottom of coastal regions in the amended model is associated with high levels of mesozooplankton biomass (the sum of medium and large zooplankton in the model), consistent with observations (Supp. Figure 6). In the coastal zone, where observed mesozooplankton biomass is highest, a three-fold increase of maximum levels of chlorophyll in the amended model sustained an ~40% increase of mesozooplankton biomass (75th percentile) compared to the baseline model. The observed cross-shore gradient of mesozooplankton biomass, ranges from a median of 2951 mg C m^{-2} in the coastal zone (n=146) to a median of 1527 mg C m^{-2} offshore (n=256) for the months June, July and August in central CCS. The amended model was able to reproduce this biomass gradient reasonably well (medians: coastal=2156 mg C m^{-2}, offshore=1211 mg C m^{-2}). This trophic connection provided an energy pathway to the highest trophic level, i.e. fish, as well as a production export pathway in the form of sinking fecal pellets.

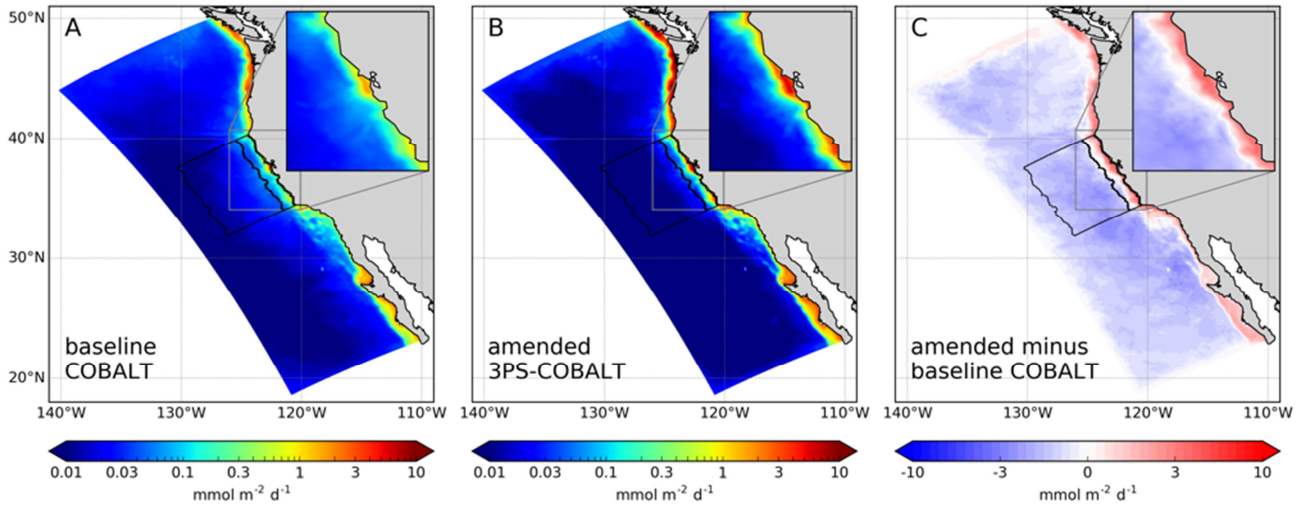

Figure 9. Summer climatological mean of benthic organic carbon flux in (A) the baseline COBALT model simulation and (B) the amended 3PS-COBALT model simulation. (C) The difference in benthic organic carbon flux between the amended and baseline model simulations.

5 Discussion

Most biogeochemical models are unable to capture the ocean's full dynamic range

of chlorophyll concentrations, especially at the high end of observations (Figure 1) (Hashioka et al. 2013). Improved spatial resolution of high resource supply areas only partly alleviates this issue (Gruber et al. 2006; Goebel et al. 2010; Gruber et al. 2011; Chenillat et al. 2013; Guo et al. 2014; Chenillat et al. 2015; Renault et al. 2016; Stock et al. 2017). Some regional models, such as the Gruber et al. 2006 – based, 1/24° resolution model used by Renault et al. (2016), are able to simulate coastal high chlorophyll levels using a single phytoplankton-grazer linkage thanks to parameter values tuned to simulate the elevated primary production during upwelling. Yet, more than half of simulated chlorophyll levels were lower than observations in the central CCS (Figure 1B). Other regional models, such as the implementation of the CoSiNE model by Guo et al. 2014, are not able to simulate coastal high chlorophyll levels (>4 mg m^{-3}) observed in the central CCS despite having multiple phytoplankton-grazer linkages (Figure 1B). Instead, we hypothesized that the poor representation of the dynamic range of chlorophyll was due to improperly resolved phytoplankton-grazer linkages and in particular to lacking model representation of large diatoms that often dominate high chlorophyll phytoplankton blooms (Venrick 2002; Irigoien et al. 2004; Taylor et al. 2012). We tested this hypothesis using an eddy-resolving (~7 km, 1/15°) ROMS model and adding a phytoplankton group with physiological characteristics and trophic links characteristic of large, chain-forming coastal diatoms. This new phytoplankton type has relatively high maximum growth rates for its individual cell size and grazer protection from smaller zooplankton groups (Smetacek 1999; Sarthou et al. 2005; Slaughter et al. 2006; Edwards et al. 2012).

The addition of a single key phytoplankton group (Figure 2B), rather than many, as has been implemented in more speciose ecological models (e.g., Follows et al. 2007; Goebel et al. 2010), is a compromise between ecological complexity and computational efficiency required of plankton community models in global Earth System Models intended for multidecadal simulations. These amendments to the community structure in the model resulted in improved simulation of high chlorophyll blooms in coastal upwelling areas while maintaining the very low chlorophyll concentrations in offshore oligotrophic regions. A critical discussion of our choices for parameterizing the new chain-forming diatom phytoplankton type is warranted here. In the amended model, we chose to limit strict adherence to mean allometric trends to parameterize the large phytoplankton group specifically as a chain-forming diatom. This limited the allometric

penalties on nutrient uptake affinities and maximum growth rates relative to moderately-sized phytoplankton while still reducing top-down control. The combination of high maximum growth rates and moderate affinities for nutrient uptake is especially suited to thriving in high resource supply environments, such as coastal upwelling systems, and is exemplified by the success of diatom species with such characteristics in coastal environments (Romeo and Fisher 1982; Estrada and Blasco 1985; Venrick 2002; Lassiter et al. 2006; Edwards et al. 2012; 2015).

Several studies have attributed the success of bloom-forming diatoms to their ability to acclimate to the prevailing environmental conditions through physiological plasticity and/or nutrient storage capability (Collos et al. 1992; Stolte and Riegman 1995; Lomas and Glibert 2000; Collos et al. 2005). These mechanisms were, however, not considered herein. A recent modelling study of a simulated upwelling event (Van Oostende et al. 2015) concluded that physiological acclimation was not a necessary condition to represent high chlorophyll bloom formation by two dominant diatom species *Thalassiosira anguste-lineata* and *Chaetoceros debilis*. In this particular study, *T. anguste-lineata* was not detected by microscopy during the first 4 days of the experiment, after which it grew exponentially, while *C. debilis* was growing exponentially by the second day (Fawcett and Ward 2011). This is consistent with the findings of Collos (1982; 1986), and suggests a decoupling of nitrate uptake and growth by the generally larger *T. anguste-lineata* cells compared to the reduced capacity for nitrate storage by *C. debilis*. Both growth strategies, however, were successful in this particular context and could be approximated by a single high maximal potential growth rate. Furthermore, in the current study, the ability for chain formation, or other implicit grazing deterring mechanism, is assumed to only bear a moderate cost in terms of light and nutrient acquisition capabilities governed by allometric principles of individual cells (Pahlow et al. 1997) while having a greater propensity for density-dependent loss through aggregation (Jackson 2001; 1990).

Another simplification of current biogeochemical models that was not considered herein but could also contribute to chlorophyll misfits is the simplified representation of zooplankton lifecycles and behavior. The lag between predator and prey in current 'NPZ' models is linked to slower intrinsic rates of grazing and subsequent growth in larger zooplankton (Hansen et al. 1997). This is unlikely, however, to fully capture emergent patterns zooplankton population

712 growth resulting from complex copepod, euphausiid, gelatinous zooplankton, and jellyfish lifecycles (Carlotti et al. 2000). Life cycle effects may be further modified by vertical migration,
714 which may effectively maintain zooplankton in upwelling regions and partly counter lags (Batchelder et al. 2002).

716

Sensitivity experiments showed that adding a third phytoplankton group that followed
718 mean allometric trends (e.g., Edwards et al. 2012) could not adequately capture high chlorophyll regions or the dominance of large phytoplankton in these regions (Supp. Figure 7 and Supp.
720 Text). This result highlights the limitations of mean allometric trends and helps explain why even simulations with highly resolved representations of the size structure of the phytoplankton
722 community (e.g., Baird and Suthers 2007; Ward et al. 2012) still struggle to capture the full dynamic range of chlorophyll concentration despite the inclusion of more than 50 plankton size
724 classes. Simulations using a high spatial resolution (1/10°), emergent community ecosystem model including 2 grazers and 78 phytoplankton species applied previously to the CCS yielded
726 coastal chlorophyll concentrations lower than SeaWiFS observations, after emerging with 8 dominant phytoplankton species (Goebel et al. 2010). These 8 emergent phytoplankton groups,
728 however, may span a narrower optimal thermal window compared to the Eppley (1972) formulation of exponential increase of growth rate with temperature in COBALT, where
730 COBALT effectively represents that continuum of phytoplankton types. Dominant phytoplankton groups often deviate significantly from mean allometric trends and these
732 deviations play important roles in defining ecological niches (Tang 1995; Smetacek 1999; Sarthou et al. 2005; Edwards et al. 2012). Our interest in improved representation of chlorophyll
734 maxima in upwelling and spring bloom systems motivated our emphasis on coastal, chain-forming diatoms. Expanding applications of global earth system models will likely require
736 consideration of similarly unique ecologies. Dinoflagellates, for example, are often implicated in harmful algal blooms in eutrophied areas (Anderson et al. 2012). While similar in size to coastal
738 diatoms, they possess a highly distinct ecology derived from widespread mixotrophy, active locomotion, and toxin production (Margalef 1978; Smayda 1997; Glibert 2016; Ward and
740 Follows 2016). In other particular instances, such as coastal systems with higher coastal turbidity and imbalanced N:P supply ratios, other traits such as low light tolerance (as proxied by

chlorophyll:C ratio) or low P tolerance may be relevant in modeling coastal blooms (e.g., Baird et al. 2013; Alvarez-Fernandez and Riegman 2014; Burson et al. 2016; Kerimoglu et al. 2017).

In addition to capturing the observed dynamic range of chlorophyll concentration, the size structure of simulated phytoplankton communities needs to be consistent with the hypothesized ecological mechanisms controlling the phytoplankton community size structure along productivity and physical disturbance gradients. Upon a more detailed examination of the results, the largest two phytoplankton classes in the 3PS-COBALT model dominated the phytoplankton biomass at high chlorophyll concentration, in accordance with observations (Supp. Figure 8) (Wilkerson et al. 2000; Lassiter et al. 2006; Goericke 2011; Taylor et al. 2012). Similar to those in situ microscopy and algal pigment-based observations, remote sensing estimates of phytoplankton size class abundance typically show a shift in community structure from a dominance of picophytoplankton at low biomass in offshore CCS regions to nano- and microphytoplankton at higher biomass in the CCS coastal zones (Supp. Figures 10, 11 and 12). There is a plethora of remote sensing algorithms that have been developed over the recent years to estimate the phytoplankton community size structure and functional types (IOCCG 2014; Mouw et al. 2017). The comparison of the amended model results with three of those remote sensing approaches covering the spectrum of community structure estimates (Kostadinov et al. 2017) is generally consistent with expectations from both explanatory hypotheses: the sequential invasion of phytoplankton size classes along a resource supply gradient, and with expectations from the transient trophic decoupling mechanisms. Discrepancies remain, however, in the degree to which large phytoplankton dominate both between simulated and remote sensing-derived estimates, and among remote sensing estimates of phytoplankton size class abundance (Supp. Table 2). The Hirata et al. (2011) chlorophyll abundance-based algorithm suggests large phytoplankton dominance in high chlorophyll regions (~80-90%) that exceeds both our model, the particulate backscattering-based estimates (Kostadinov and Siegel 2009; Kostadinov 2016) and the absorption-based estimates (Roy et al. 2013), all of which distribute phytoplankton biomass more evenly between nano- and micro-sized classes in coastal regions (Supp. Figures 10, 11 and 12).

772 The discrepancies between remote sensing estimates likely stem from differences in the operational definition of the different size classes, the imperfect reflection of the true size of
774 phytoplankton classes based on pigment grouping (e.g., the cyanobacteria *Trichodesmium* spp.) (Vidussi et al. 2001), and the limited calibration of the algorithm of Hirata et al. (2011) at
776 chlorophyll concentrations >5 mg m^{-3}. Furthermore, the particle backscattering-based algorithm of Kostadinov et al. (2009; 2016) not only includes phytoplankton but other similarly sized
778 particles, such as heterotrophic bacteria, microzooplankton, and detritus. This could be why the algorithm of Kostadinov et al. (2016) appears to overestimate the biomass fraction of
780 picophytoplankton compared to that of Hirata et al. (2011), which is in closer agreement with the amended model. Moreover, Kostadinov et al. (2016) acknowledged that their single conversion
782 factor for determining the fraction of living phytoplankton carbon from total POC may not reflect the variability of trophic status of plankton communities across ocean regions.

784

The realization of high chlorophyll concentrations in this study may in part be due to the
786 effective number of 'sequential invasions' a model can accommodate, which is likely a function of the range of size classes grazed by a zooplankton group relative to the range of available
788 phytoplankton groups. A higher diversity of phytoplankton groups favors invasion of different niches (Irwin et al. 2006) along environmental gradients, but phytoplankton blooms
790 characterized by the accumulation of biomass may only occur through temporal or spatial decoupling of trophic control (Irigoien et al. 2005). A time series centered around an upwelling
792 event ~75 km off the central California coast demonstrates the succession of phytoplankton groups during the bloom response (Supp. Figure 9). In this time series example, the dominant
794 phytoplankton size class contributing to primary production switches from mostly small phytoplankton to the two largest size classes (Supp. Figure 9B). The losses of the dominant
796 phytoplankton groups, due to grazing and aggregation, follow their growth patterns during this transient nutrient supply event (Supp. Figures 9C and 9D). These results are consistent with the
798 'sequential invasion' and transient 'grazer decoupling' mechanisms implied by the amended model structure, even though the relative importance of each of these non-mutually exclusive
800 mechanisms could not be partitioned using the experimental set-up in this study.

A key biogeochemical consequence of improved representation of high coastal chlorophyll concentration is the intensification of carbon export in coastal regions (Figure 9). Modeled sinking organic matter particles are composed of both mesozooplankton-derived fecal pellets and phytoplankton-derived detritus formed by aggregation. Sinking of these particles transfers organic matter to depth, strengthens the biological pump and results in higher pe-ratios near the coast. This is consistent with global syntheses and theory (Dunne et al. 2005, and references therein; Mouw et al. 2016), though we note that evidence for increased sinking particle flux along increasing productivity gradients in the CCS has been surprisingly equivocal (Stukel and Ohman 2013). Increased particle sinking flux over intensely productive nearshore regions, however, appears consistent with widespread hypoxic conditions (Figures 7 and 8).

Capturing the higher export flux after including the chain-forming diatom allowed improved simulation of near-bottom oxygen levels on the continental shelf and shelf slope, especially the occurrence of hypoxic events on the shelf, through intensification of the model's coastal nutrient trapping (Najjar et al. 1992; Aumont et al. 1999). This productivity and export flux-driven decline of oxygen on the shelf has been found to be the result of a combination of local respiration of organic matter and circulation processes (Hales et al. 2006; Siedlecki et al. 2015). Besides a direct link to the respiration of sinking organic matter, the oxygen and nutrient content of the upwelled waters fueling the productive coastal blooms in the first place can have a strong influence on the occurrence of seasonal shelf hypoxia (Grantham et al. 2004). Higher nutrient input to the surface shelf waters can result in higher primary production and stronger respiration of the exported organic material, depleting dissolved oxygen near the shelf bottom (Wheeler and Huyer 2003). This effect can be compounded when the nutrient rich deeper water masses being upwelled have an already lowered oxygen content due to their biogeochemical history and origin (Freeland et al. 2003). These hypoxic episodes seem to have become more frequent since the year 2000 in the northern CCS (Chan et al. 2008) and the hypoxic boundary has been shoaling in recent decades in the southern CCS (Bograd et al. 2008), affecting the survival and the habitat range of benthic as well as mesopelagic fishes and invertebrates (Stewart et al. 2012; Keller et al. 2015).

832 Improvements in dynamical climate prediction models have allowed for predictions of climate variables (e.g., temperature, dissolved oxygen and carbon dioxide concentration, 834 productivity) at scales that are relevant to the understanding and management of living marine resources (Tommasi et al. 2017). Forecasts of these climate variables from weeks to years have 836 been useful to the anticipatory management of fisheries resources or aquaculture industries and their associated supply chains (Stock et al. 2011; Mills et al. 2013; Stock et al. 2015; Siedlecki et 838 al. 2016). Along the California Current, uncertainty about the future frequency of invasion of the northern CCS by subarctic water masses or advection of low dissolved oxygen water, timing of 840 upwelling in the northern CCS and stratification in the southern CCS (Freeland et al. 2003; Mackas et al. 2006; Rykaczewski and Dunne 2010; Rykaczewski et al. 2015) hampers prediction 842 of coastal productivity, community composition and dissolved oxygen levels. This model provides a framework to test hypotheses about the ecological consequences of such system-level 844 perturbations (Dussin et al. in prep.), with the goal of supporting climate prediction and resource management decisions.

846

6 Conclusions

848

Modeling of chlorophyll concentration and subsurface oxygen from productive coastal 850 upwelling to oligotrophic systems can be greatly improved by including a better representation of ecological succession mechanisms. The full dynamic range of observed chlorophyll 852 concentration, representative of the global ocean, was successfully simulated, specifically by elevating simulated coastal chlorophyll concentration. This was accomplished by adding a 854 functional phytoplankton group representing large, chain-forming coastal diatoms and allowing for transient trophic decoupling between the added phytoplankton group and the grazer 856 functional group representing large copepods and krill. High relative abundance of large phytoplankton at high productivity corroborates sequential invasion and transient trophic 858 decoupling as the ecological mechanisms at work. An improved simulation of the coastal bloom magnitude and community composition allowed the model to reproduce observed spatial patterns 860 of near-bottom dissolved oxygen across the western United States' continental shelf. Accurate simulation of the phytoplankton-derived export flux driving the consumption of oxygen on the

shelf bottom is crucial to predict the frequency and magnitude of hypoxic events, which are detrimental to benthic fauna and demersal fish. This regional model provides a framework to investigate the frequency and intensity of these hypoxic events on the shelf and the compounding effect of high nutrient-low oxygen content upwelled water masses. These model improvements come at a modest complexity cost making it possible to apply the amended model's ecological structure to global biogeochemical simulations of the ocean.

7 Acknowledgements

This research was made possible by funding of NVO and RD from the Cooperative Institute for Climate Science (Princeton University) and NOAA award NA-15OAR4310133 to EC. We thank the NWFSC bottom trawl survey group and associated partners for producing and making the near bottom oxygen data available, F. Chavez and R. Michisaki from the Biological Oceanography Group at MBARI for collecting, processing and making available the CalCOFI line 67 data, NASA Goddard Space Flight Center, Ocean Biology Processing Group for making Sea-viewing Wide Field-of-view Sensor Ocean Color Data available, and L. Guo, F. Chenillat, and L. Renault for sharing their regional model chlorophyll data. We are grateful to the three anonymous reviewers for their valuable comments which improved this manuscript.

8 Bibliography

Aksnes, D. L., and J. K. Egge. 1991. A theoretical-model for nutrient-uptake in phytoplankton. Mar. Ecol.-Prog. Ser. **70**: 65–72. doi:10.3354/meps070065

Alvarez-Fernandez, S., and R. Riegman. 2014. Chlorophyll in North Sea coastal and offshore waters does not reflect long term trends of phytoplankton biomass. J. Sea Res. **91**: 35–44.

Anderson, D. M., A. D. Cembella, and G. M. Hallegraeff. 2012. Progress in understanding harmful algal blooms: paradigm shifts and new technologies for research, monitoring, and management. Annual review of … **4**: 143–176. doi:10.1146/annurev-marine-120308-081121

Armstrong, R. A. 1994. Grazing limitation and nutrient limitation in marine ecosystems: steady state solutions of an ecosystem model with multiple food chains. Limnol. Oceanogr.

Aumont, O., and L. Bopp. 2006. Globalizing results from ocean in situ iron fertilization studies. Glob. Biogeochem. Cycle **20**. doi:10.1029/2005GB002591

Aumont, O., J. C. Orr, P. Monfray, G. Madec, and E. Maier-Reimer. 1999. Nutrient trapping in the equatorial Pacific: The ocean circulation solution. Glob. Biogeochem. Cycle **13**: 351–369. doi:10.1029/1998GB900012

Baird, M. E., and I. M. Suthers. 2007. A size-resolved pelagic ecosystem model. Ecological Modelling **203**: 185–203. doi:10.1016/j.ecolmodel.2006.11.025

Baird, M. E., P. J. Ralph, F. Rizwi, K. Wild-Allen, and A. D. L. Steven. 2013. A dynamic model of the cellular carbon to chlorophyll ratio applied to a batch culture and a continental shelf ecosystem. Limnol. Oceanogr. **58**: 1215–1226. doi:10.4319/lo.2013.58.4.1215

Banse, K. 1982. Cell volumes, maximal growth rates of unicellular algae and ciliates, and the role of ciliates in the marine pelagial. Limnol. Oceanogr. **27**: 1059–1071. doi:10.4319/lo.1982.27.6.1059

Barber, R. T., and M. R. Hiscock. 2006. A rising tide lifts all phytoplankton: Growth response of other phytoplankton taxa in diatom-dominated blooms. Glob. Biogeochem. Cycle **20**. doi:10.1029/2006gb002726

Batchelder, H. P., C. A. Edwards, and T. M. Powell. 2002. Individual-based models of copepod populations in coastal upwelling regions: implications of physiologically and environmentally influenced diel vertical migration on demographic success and nearshore retention. Prog. Oceanogr. **53**: 307–333.

Bissinger, J. E., D. J. S. Montagnes, J. Sharples, and D. Atkinson. 2008. Predicting marine phytoplankton maximum growth rates from temperature: Improving on the Eppley curve using quantile regression. Limnol. Oceanogr. **53**: 487–493. doi:10.4319/lo.2008.53.2.0487

Bograd, S. J., C. G. Castro, and E. Di Lorenzo. 2008. Oxygen declines and the shoaling of the hypoxic boundary in the California Current. Geophysical …. doi:10.1029/2008GL034185

Brown, J. H., J. F. Gillooly, A. P. Allen, V. M. Savage, and G. B. West. 2004. Toward a metabolic theory of ecology. Ecology **85**: 1771–1789. doi:10.1890/03-9000

Burson, A., M. Stomp, L. Akil, C. P. D. Brussaard, and J. Huisman. 2016. Unbalanced reduction of nutrient loads has created an offshore gradient from phosphorus to nitrogen limitation in the North Sea. Limnol. Oceanogr. **61**: 869–888. doi:10.1002/lno.10257

Carlotti, F., J. Giske, and F. Werner. 2000. Modeling zooplankton dynamics, p. 571–667. *In* R. Harris, P. Wiebe, J. Lenz, H.R. Skjoldal, and M. Huntley [eds.], ICES Zooplankton Methodology Manual. Elsevier.

Carton, J. A., and B. S. Giese. 2008. A Reanalysis of Ocean Climate Using Simple Ocean Data Assimilation (SODA). Monthly Weather Review **136**: 2999–3017. doi:10.1175/2007MWR1978.1

Chai, F., R. C. Dugdale, T. H. Peng, F. P. Wilkerson, and R. T. Barber. 2002. One-dimensional ecosystem model of the equatorial Pacific upwelling system. Part I: model development and silicon and nitrogen cycle. Deep-Sea Res. Part II-Top. Stud. Oceanogr. **49**: 2713–2745.

Chan, F., J. A. Barth, J. Lubchenco, A. Kirincich, H. Weeks, W. T. Peterson, and B. A. Menge. 2008. Emergence of anoxia in the California current large marine ecosystem. Science **319**: 920–920. doi:10.1126/science.1149016

Chavez, F. P. 1989. Size distribution of phytoplankton in the central and eastern tropical Pacific. Glob. Biogeochem. Cycle **3**: 27–35.

Chenillat, F., P. J. S. Franks, P. Rivière, X. Capet, N. Grima, and B. Blanke. 2015. Plankton dynamics in a cyclonic eddy in the Southern California Current System. J. Geophys. Res.-Oceans **120**: 5566–5588. doi:10.1002/2015JC010826

Chenillat, F., P. Rivière, X. Capet, P. J. S. Franks, and B. Blanke. 2013. California Coastal Upwelling Onset Variability: Cross-Shore and Bottom-Up Propagation in the Planktonic Ecosystem S.J. Bograd [ed.]. PLoS One **8**: e62281–15. doi:10.1371/journal.pone.0062281

Chisholm, S. W. 1992. Phytoplankton Size, p. 213–237. *In* P.G. Falkowski, A.D. Woodhead, and K. Vivirito [eds.], Primary Productivity and Biogeochemical Cycles in the Sea. Springer US.

Christensen, J. P., W. M. Smethie, and A. H. Devol. 1987. Benthic nutrient regeneration and denitrification on the Washington continental shelf. Deep-Sea Res. Part I-Oceanogr. Res. Pap. **34**: 1027–1047.

Claustre, H. 1994. The trophic status of various oceanic provinces as revealed by phytoplankton pigment signatures. Limnol. Oceanogr. **39**: 1206–1210. doi:10.4319/lo.1994.39.5.1206

Collos, Y. 1982. Transient situations in nitrate assimilation by marine diatoms - short-term uncoupling of nitrate uptake and reduction. J. Exp. Mar. Biol. Ecol. **62**: 285–295. doi:10.1016/0022-0981(82)90208-8

Collos, Y. 1986. Time-lag algal growth dynamics - biological constraints on primary production in aquatic environments. Mar. Ecol.-Prog. Ser. **33**: 193–206. doi:10.3354/meps033193

Collos, Y., A. Vaquer, and P. Souchu. 2005. Acclimation of nitrate uptake by phytoplankton to high substrate levels. J. Phycol. **41**: 466–478. doi:10.1111/j.1529-8817.2005.00067.x

Collos, Y., M. Y. Siddiqi, M. Y. Wang, A. D. M. Glass, and P. J. Harrison. 1992. Nitrate uptake kinetics by two marine diatoms using the radioactive tracer 13N. J. Exp. Mar. Biol. Ecol. **163**: 251–260. doi:10.1016/0022-0981(92)90053-d

Curchitser, E. N., D. B. Haidvogel, A. J. Hermann, E. L. Dobbins, T. M. Powell, and A. Kaplan. 2005. Multi-scale modeling of the North Pacific Ocean: Assessment and analysis of simulated basin-scale variability (1996–2003). Journal of Geophysical Research **110**. doi:10.1029/2005JC002902

Dai, A., and K. E. Trenberth. 2002. Estimates of Freshwater Discharge from Continents: Latitudinal and Seasonal Variations. Journal of Hydrometeorology **3**: 660–687. doi:10.1175/1525-7541(2002)003<0660:EOFDFC>2.0.CO;2

DeVries, T., C. Deutsch, F. O. Primeau, B. Chang, and A. Devol. 2012. Global rates of water-column denitrification derived from nitrogen gas measurements. Nature Geosci **5**: 547–550. doi:10.1038/ngeo1515

Doney, S. C., D. M. Glover, and R. G. Najjar. 1996. A new coupled, one-dimensional biological-physical model for the upper ocean: Applications to the JGOFS Bermuda Atlantic Time-series Study (BATS) site. Deep Sea Research Part II: Topical … **43**: 591–624. doi:10.1016/0967-0645(95)00104-2

Dufresne, J. L., M. A. Foujols, S. Denvil, A. Caubel, and O. Marti. 2013. Climate change projections using the IPSL-CM5 Earth System Model: from CMIP3 to CMIP5. Climate Dynamics. doi:10.1007/s00382-012-1636-1

Dunne, J. P., J. G. John, A. J. Adcroft, and S. M. Griffies. 2012. GFDL's ESM2 global coupled climate-carbon Earth System Models. Part I: Physical formulation and baseline simulation characteristics. Journal of …. doi:10.1175/JCLI-D-11-00560.1

Dunne, J. P., J. G. John, E. Shevliakova, and others. 2013. GFDL's ESM2 Global Coupled Climate-Carbon Earth System Models. Part II: Carbon System Formulation and Baseline Simulation Characteristics. J. Climate **26**: 2247–2267. doi:10.1175/jcli-d-12-00150.1

Dunne, J. P., R. A. Armstrong, A. Gnanadesikan, and J. L. Sarmiento. 2005. Empirical and mechanistic models for the particle export ratio. Glob. Biogeochem. Cycle **19**: 16. doi:10.1029/2004gb002390

Edwards, K. F., M. K. Thomas, C. A. Klausmeier, and E. Litchman. 2012. Allometric scaling and taxonomic variation in nutrient utilization traits and maximum growth rate of phytoplankton. Limnol. Oceanogr. **57**: 554–566. doi:10.4319/lo.2012.57.2.0554

Edwards, K. F., M. K. Thomas, C. A. Klausmeier, and E. Litchman. 2015. Light and growth in marine phytoplankton: allometric, taxonomic, and environmental variation. Limnol. Oceanogr. **60**: 540–552. doi:10.1002/lno.10033

Elrod, V. A., W. M. Berelson, K. H. Coale, and K. S. Johnson. 2004. The flux of iron from continental shelf sediments: A missing source for global budgets. Geophys. Res. Lett. **31**. doi:10.1029/2004GL020216

Eppley, R. W. 1972. Temperature and phytoplankton growth in sea. Fishery Bulletin **70**: 1063–1085.

Eppley, R. W., and B. J. Peterson. 1979. Particulate organic-matter flux and planktonic new production in the deep ocean. Nature **282**: 677–680. doi:10.1038/282677a0

Eppley, R. W., and E. H. Renger. 1974. Nitrogen assimilation of an oceanic diatom in nitrogen-limited continuous culture. Journal of Phycology **10**: 15–23. doi:10.1111/j.1529-8817.1974.tb02671.x

Eppley, R. W., J. N. Rogers, and J. J. McCarthy. 1969. Half-saturation constants for uptake of nitrate and ammonium by marine phytoplankton. Limnol. Oceanogr. **14**: 912–920.

Estrada, M., and D. Blasco. 1985. Phytoplankton assemblages in coastal upwelling areas, p. 379–402. *In* C. Bas, R. Margalef, and P. Rubias [eds.], International symposium of upwelling of Western Africa. Instituto de Investigaciones Pesqueras.

Fan, S.-M., W. J. Moxim, and H. Levy. 2006. Aeolian input of bioavailable iron to the ocean. Geophys. Res. Lett. **33**. doi:10.1029/2005GL024852

Fawcett, S. E., and B. B. Ward. 2011. Phytoplankton succession and nitrogen utilization during the development of an upwelling bloom. Mar. Ecol.-Prog. Ser. **428**: 13–31. doi:10.3354/meps09070

Follows, M. J., S. Dutkiewicz, S. Grant, and S. W. Chisholm. 2007. Emergent biogeography of microbial communities in a model ocean. Science **315**: 1843–1846. doi:10.1126/science.1138544

Franks, P. J. S. 2001. Phytoplankton blooms in a fluctuating environment: the roles of plankton response time scales and grazing. J. Plankton Res. **23**: 1433–1441. doi:10.1093/plankt/23.12.1433

Freeland, H. J., G. Gatien, and A. Huyer. 2003. Cold halocline in the northern California Current: An invasion of subarctic water. Geophysical Research …. doi:10.1029/2002GL016663

Friedland, K. D., C. Stock, K. F. Drinkwater, and others. 2012. Pathways between Primary Production and Fisheries Yields of Large Marine Ecosystems K.I. Stergiou [ed.]. PLoS One **7**. doi:10.1371/journal.pone.0028945

Frost, B. W., and N. C. Franzen. 1992. Grazing and iron limitation in the control of phytoplankton stock and nutrient concentration - a chemostat analog of the pacific equatorial upwelling zone. Mar. Ecol.-Prog. Ser. **83**: 291–303. doi:10.3354/meps083291

Fuchs, H. L., and P. Franks. 2010. Plankton community properties determined by nutrients and size-selective feeding. Mar. Ecol.-Prog. Ser. doi:10.2307/24875175

Garcia, H. E., R. A. Locarnini, T. P. Boyer, O. K. Baranova, M. M. Zweng, J. R. Reagan, and D. R. Johnson. 2013. World Ocean Atlas 2013. Volume 4: Dissolved Inorganic Nutrients (phospate, nitrate, silicate), S. Levitus and M. A [eds.]. NOAA Atlas NESDIS 76.

Geider, R. J. 1993. Quantitative phytoplankton physiology: implications for primary production and phytoplankton growth. ICES Mar Sci Symp **197**: 52–62.

Geider, R. J., H. L. MacIntyre, and T. M. Kana. 1997. Dynamic model of phytoplankton growth and acclimation: Responses of the balanced growth rate and the chlorophyll a:carbon ratio to light, nutrient-limitation and temperature. Mar. Ecol.-Prog. Ser. **148**: 187–200. doi:10.3354/meps148187

Giorgetta, M. A., J. Jungclaus, C. H. Reick, and others. 2013. Climate and carbon cycle changes from 1850 to 2100 in MPI-ESM simulations for the Coupled Model Intercomparison Project phase 5. J. Adv. Model. Earth Syst. **5**: 572–597. doi:10.1002/jame.20038

Glibert, P. M. 2016. Margalef revisited: A new phytoplankton mandala incorporating twelve dimensions, including nutritional physiology. Harmful Algae **55 IS -**: 25–30.

Goebel, N. L., C. A. Edwards, J. P. Zehr, and M. J. Follows. 2010. An emergent community ecosystem model applied to the California Current System. J. Mar. Syst. **83**: 221–241. doi:10.1016/j.jmarsys.2010.05.002

Goericke, R. 2011. The structure of marine phytoplankton communities -patterns, rules and mechanisms. CalCOFI Rep. **52**: 182–197.

Gordon, H. R., and W. R. McCluney. 1975. Estimation of the Depth of Sunlight Penetration in the Sea for Remote Sensing. Appl. Opt. **14**: 413–416.

Grantham, B. A., F. Chan, K. J. Nielsen, D. S. Fox, and J. A. Barth. 2004. Upwelling-driven nearshore hypoxia signals ecosystem and oceanographic changes in the northeast Pacific. Nature. doi:10.1038/nature02605

Gruber, N., H. Frenzel, S. C. Doney, and others. 2006. Eddy-resolving simulation of plankton ecosystem dynamics in the California Current System. Deep-Sea Res. Part I-Oceanogr. Res. Pap. **53**: 1483–1516. doi:10.1016/j.dsr.2006.06.005

Gruber, N., Z. Lachkar, H. Frenzel, P. Marchesiello, M. Münnich, J. C. McWilliams, T. Nagai, and G.-K. Plattner. 2011. Eddy-induced reduction of biological production in eastern boundary upwelling systems. Nature Publishing Group **4**: 787–792. doi:10.1038/ngeo1273

Guo, L., F. Chai, P. Xiu, H. Xue, S. Rao, Y. Liu, and F. P. Chavez. 2014. Seasonal dynamics of physical and biological processes in the central California Current System: A modeling study. Ocean Dynamics **64**: 1137–1152. doi:10.1007/s10236-014-0721-x

Hales, B., L. Karp-Boss, A. Perlin, and P. A. Wheeler. 2006. Oxygen production and carbon sequestration in an upwelling coastal margin. Glob. Biogeochem. Cycle **20**: n/a–n/a. doi:10.1029/2005GB002517

Hansen, B., P. K. Bjørnsen, and P. J. Hansen. 1994. The size ratio between planktonic predators and their prey. Limnol. Oceanogr. **39**: 395–403. doi:10.4319/lo.1994.39.2.0395

Hansen, P. J., P. K. Bjørnsen, and B. W. Hansen. 1997. Zooplankton grazing and growth: Scaling within the 2-2,000-µm body size range. Limnol. Oceanogr. **42**: 687–704. doi:10.4319/lo.1997.42.4.0687

Hashioka, T., M. Vogt, Y. Yamanaka, and others. 2013. Phytoplankton competition during the spring bloom in four plankton functional type models. Biogeosciences **10**: 6833–6850. doi:10.5194/bg-10-6833-2013

Hermann, A. J., E. N. Curchitser, D. B. Haidvogel, and E. L. Dobbins. 2009. A comparison of remote vs. local influence of El Niño on the coastal circulation of the northeast Pacific. Deep-Sea Res. Part II-Top. Stud. Oceanogr. **56**: 2427–2443.

Hirata, T., N. J. Hardman-Mountford, R. J. W. Brewin, and others. 2011. Synoptic relationships between surface Chlorophyll-a and diagnostic pigments specific to phytoplankton functional types. Biogeosciences **8**: 311–327. doi:10.5194/bg-8-311-2011

Hurrell, J. W., M. M. Holland, and P. R. Gent. 2013. The community earth system model: a framework for collaborative research. Bulletin of the …. doi:10.1175/BAMS-D-12-00121.1

Ilyina, T., K. D. Six, J. Segschneider, E. Maier-Reimer, H. Li, and I. Núñez-Riboni. 2013. Global ocean biogeochemistry model HAMOCC: Model architecture and performance as component of the MPI-Earth system model in different CMIP5 experimental realizations. J. Adv. Model. Earth Syst. **5**: 287–315. doi:10.1029/2012MS000178

Ingrid, G., T. Andersen, and O. Vadstein. 1996. Pelagic food webs and eutrophication of coastal waters: Impact of grazers on algal communities. Marine Pollution Bulletin **33**: 22–35.

IOCCG. 2014. Phytoplankton Functional Types from Space. Reports of the International Ocean-Colour Coordinating Group. 15. 15.

Irigoien, X., J. Huisman, and R. P. Harris. 2004. Global biodiversity patterns of marine phytoplankton and zooplankton. Nature **429**: 863–867. doi:10.1038/nature02593

Irigoien, X., K. J. Flynn, and R. P. Harris. 2005. Phytoplankton blooms: a “loophole” in microzooplankton grazing impact? J. Plankton Res. **27**: 313–321. doi:10.1093/plankt/fbi011

Irwin, A. J., Z. V. Finkel, O. M. E. Schofield, and P. G. Falkowski. 2006. Scaling-up from nutrient physiology to the size-structure of phytoplankton communities. J. Plankton Res. **28**: 459–471. doi:10.1093/plankt/fbi148

Jackson, G. A. 2001. Effect of coagulation on a model planktonic food web. Deep-Sea Res. Part I-Oceanogr. Res. Pap. **48**: 95–123. doi:10.1016/S0967-0637(00)00040-6

Jackson, G. A. 1990. A model of the formation of marine algal flocs by physical coagulation processes. Deep-Sea Res. Part I-Oceanogr. Res. Pap. **37**: 1197–1211. doi:10.1016/0198-0149(90)90038-W

Kahru, M., R. Kudela, C. Anderson, M. Manzano-Sarabia, and B. Mitchell. 2014. Evaluation of Satellite Retrievals of Ocean Chlorophyll-a in the California Current. Remote Sensing **6**: 8524–8540. doi:10.3390/rs6098524

Keller, A. A., L. Ciannelli, and W. W. Wakefield. 2015. Occurrence of demersal fishes in relation to near-bottom oxygen levels within the California Current large marine ecosystem. Fisheries …. doi:10.1111/fog.12100

Kerimoglu, O., R. Hofmeister, J. Maerz, R. Riethmüller, and K. W. Wirtz. 2017. The acclimative biogeochemical model of the southern North Sea. Biogeosciences **14**: 4499–4531.

Key, R. M., A. Kozyr, C. L. Sabine, and others. 2004. A global ocean carbon climatology: Results from Global Data Analysis Project (GLODAP). Glob. Biogeochem. Cycle **18**: 1–23. doi:10.1029/2004GB002247

Kishi, M. J., M. Kashiwai, D. M. Ware, and others. 2007. NEMURO—a lower trophic level model for the North Pacific marine ecosystem. Ecological Modelling **202**: 12–25.

Kostadinov, T. S. 2016. Carbon-based phytoplankton size classes retrieved via ocean color estimates of the particle size distribution. Ocean Science. doi:10.5194/os-12-561-2016

Kostadinov, T. S., A. Cabré, H. Vedantham, and others. 2017. Inter-comparison of phytoplankton functional type phenology metrics derived from ocean color algorithms and Earth System Models. Remote Sensing of Environment **190**: 162–177.

Kostadinov, T. S., and D. A. Siegel. 2009. Retrieval of the particle size distribution from satellite ocean color observations. Journal of Geophysical …. doi:10.1029/2009JC005303

Kretzschmar, M., R. M. Nisbet, and E. Mccauley. 1993. A Predator-Prey Model for Zooplankton Grazing on Competing Algal Populations. Theoretical Population Biology **44**: 32–66.

Landry, M., and A. Calbet. 2004. Microzooplankton production in the oceans. ICES Journal of Marine Science **61**: 501–507. doi:10.1016/j.icesjms.2004.03.011

Large, W. G., and S. G. Yeager. 2004. Diurnal to decadal global forcing for ocean and sea-ice models: the data sets and flux climatologies.

Lassiter, A. M., F. P. Wilkerson, R. C. Dugdale, and V. E. Hogue. 2006. Phytoplankton assemblages in the CoOP-WEST coastal upwelling area. Deep-Sea Res. Part II-Top. Stud. Oceanogr. **53**: 3063–3077. doi:10.1016/j.dsr2.2006.07.013

Leibold, M. A. 1996. A Graphical Model of Keystone Predators in Food Webs: Trophic Regulation of Abundance, Incidence, and Diversity Patterns in Communities. The American Naturalist **147**: 784–812. doi:10.1086/285879

Lévy, M., R. Ferrari, and P. Franks. 2012. Bringing physics to life at the submesoscale. Geophysical … **39**. doi:10.1029/2012GL052756

Lindsay, K., G. B. Bonan, and S. C. Doney. 2014. Preindustrial-control and twentieth-century carbon cycle experiments with the Earth system model CESM1 (BGC). Journal of …. doi:10.1175/JCLI-D-12-00565.1

Lomas, M. W., and P. M. Glibert. 2000. Comparisons of nitrate uptake, storage, and reduction in marine diatoms and flagellates. J. Phycol. **36**: 903–913. doi:10.1046/j.1529-8817.2000.99029.x

Lomas, M. W., J. A. Bonachela, S. A. Levin, and A. C. Martiny. 2014. Impact of ocean phytoplankton diversity on phosphate uptake. Proceedings of the National Academy of Sciences **111**: 17540–17545. doi:10.1073/pnas.1420760111

Longhurst, A. 2007. Ecological Geography of the Sea, Academic Press.

Longhurst, A., S. Sathyendranath, T. Platt, and C. Caverhill. 1995. An estimate of global primary production in the ocean from satellite radiometer data. J. Plankton Res. **17**: 1245–1271. doi:10.1093/plankt/17.6.1245

Mackas, D. L., W. T. Peterson, M. D. Ohman, and B. E. Lavaniegos. 2006. Zooplankton anomalies in the California Current system before and during the warm ocean conditions of 2005. Geophys. Res. Lett. **33**: n/a–n/a. doi:10.1029/2006GL027930

Manizza, M., C. Le Quéré, A. J. Watson, and E. T. Buitenhuis. 2005. Bio-optical feedbacks among phytoplankton, upper ocean physics and sea-ice in a global model. Geophys. Res. Lett. **32**. doi:10.1029/2004GL020778

Marañón, E., P. Cermeño, D. C. López-Sandoval, T. Rodriguez-Ramos, C. Sobrino, M. Huete-Ortega, J. M. Blanco, and J. Rodriguez. 2013. Unimodal size scaling of phytoplankton growth and the size dependence of nutrient uptake and use. Ecol. Lett. **16**: 371–379. doi:10.1111/ele.12052

Margalef, R. 1978. Life-forms of phytoplankton as survival alternatives in an unstable environment. Oceanol. Acta **1**: 493–509.

Martin-Jezequel, V., M. Hildebrand, and M. A. Brzezinski. 2000. Silicon metabolism in diatoms: Implications for growth. J. Phycol. **36**: 821–840. doi:10.1046/j.1529-8817.2000.00019.x

Mills, K. E., A. J. Pershing, C. J. Brown, and others. 2013. Fisheries management in a changing climate: lessons from the 2012 ocean heat wave in the Northwest Atlantic. Oceanography **26**: 191–195.

Moloney, C. L., and J. G. Field. 1989. General allometric equations for rates of nutrient uptake, ingestion, and respiration in plankton organisms. Limnol. Oceanogr. **34**: 1290–1299. doi:10.4319/lo.1989.34.7.1290

Moloney, C. L., and J. G. Field. 1991. The size-based dynamics of plankton food webs. I. A simulation model of carbon and nitrogen flows. J. Plankton Res. **13**: 1003–1038. doi:10.1093/plankt/13.5.1003

Moore, J. K., S. C. Doney, J. A. Kleypas, D. M. Glover, and I. Y. Fung. 2001. An intermediate complexity marine ecosystem model for the global domain. Deep-Sea Res. Part II-Top. Stud. Oceanogr. **49**: 403–462.

Morel, A., and A. Bricaud. 1981. Theoretical results concerning light absorption in a discrete medium, and application to specific absorption of phytoplankton. Deep Sea Research Part A Oceanographic Research …. doi:10.1016/0198-0149(81)90039-X

Moriarty, R., and T. D. O'Brien. 2013. Distribution of mesozooplankton biomass in the global ocean. Earth System Science Data **5**: 45–55. doi:10.1594/PANGAEA.785501

Mouw, C. B., A. Barnett, G. A. McKinley, L. Gloege, and D. Pilcher. 2016. Global ocean particulate organic carbon flux merged with satellite parameters. Earth Syst. Sci. Data **8**: 531–541.

Mouw, C. B., N. J. Hardman-Mountford, S. Alvain, and others. 2017. A Consumer's Guide to Satellite Remote Sensing of Multiple Phytoplankton Groups in the Global Ocean. Front. Mar. Sci. **4**: 497. doi:10.3389/fmars.2017.00041

Moxim, W. J., S.-M. Fan, and H. Levy. 2011. The meteorological nature of variable soluble iron transport and deposition within the North Atlantic Ocean basin. Journal of Geophysical Research: Oceans **116**. doi:10.1029/2010JD014709

Munk, W. H., and G. A. Riley. 1952. Absorption of nutrients by aquatic plants. J. Mar. Res. **11**: 215–240.

Najjar, R. G., J. L. Sarmiento, and J. R. Toggweiler. 1992. Downward transport and fate of organic matter in the ocean: Simulations with a general circulation model. Glob. Biogeochem. Cycle **6**: 45–76. doi:10.1029/91GB02718

Omand, M. M., E. A. D'Asaro, C. M. Lee, M. J. Perry, N. Briggs, I. Cetinić, and A. Mahadevan. 2015. Eddy-driven subduction exports particulate organic carbon from the spring bloom. Science **348**: 222–225. doi:10.1126/science.1260062

Pahlow, M., U. Riebesell, and D. A. Wolf-Gladrow. 1997. Impact of cell shape and chain formation on nutrient acquisition by marine diatoms. Limnol. Oceanogr. **42**: 1660–1672. doi:10.4319/lo.1997.42.8.1660

Powell, T. M., C. V. W. Lewis, E. N. Curchitser, D. B. Haidvogel, A. J. Hermann, and E. L. Dobbins. 2006. Results from a three-dimensional, nested biological-physical model of the California Current System and comparisons with statistics from satellite imagery. Journal of Geophysical Research **111**. doi:10.1029/2004JC002506

Raimbault, P., M. Rodier, and I. Taupier-Letage. 1988. Size fraction of phytoplankton in the Ligurian Sea and the Algerian Basin (Mediterranean Sea): Size distribution versus total concentration. Marine Microbial Food Webs **3**: 1–7.

Raven, J. A. 1998. The twelfth Tansley Lecture. Small is beautiful: the picophytoplankton. Funct Ecology **12**: 503–513.

Renault, L., C. Deutsch, J. C. McWilliams, H. Frenzel, J.-H. Liang, and F. Colas. 2016. Partial decoupling of primary productivity from upwelling in the California Current system. Nature Geoscience **9**: 505–508. doi:10.1038/ngeo2722

Reynolds, R. W., T. M. Smith, C. Liu, D. B. Chelton, K. S. Casey, and M. G. Schlax. 2007. Daily High-Resolution-Blended Analyses for Sea Surface Temperature. J. Climate **20**: 5473–5496. doi:10.1175/2007JCLI1824.1

Romagnan, J. B., L. Legendre, L. Guidi, and J. L. Jamet. 2015. Comprehensive model of annual plankton succession based on the whole-plankton time series approach. PLoS One. doi:10.1371/journal.pone.0119219

Romeo, A. J., and N. S. Fisher. 1982. Intraspecific Comparisons of Nitrate Uptake in 3 Marine Diatoms. J. Phycol. **18**: 220–225.

Roy, S., S. Sathyendranath, H. Bouman, and T. Platt. 2013. The global distribution of phytoplankton size spectrum and size classes from their light-absorption spectra derived from satellite data. Remote Sensing of Environment **139**: 185–197. doi:10.1016/j.rse.2013.08.004

Rykaczewski, R. R., and J. P. Dunne. 2010. Enhanced nutrient supply to the California Current Ecosystem with global warming and increased stratification in an earth system model. Geophys. Res. Lett. **37**.

Rykaczewski, R. R., J. P. Dunne, W. J. Sydeman, M. García Reyes, B. A. Black, and S. J. Bograd. 2015. Poleward displacement of coastal upwelling-favorable winds in the ocean's eastern boundary currents through the 21st century. Geophys. Res. Lett. **42**: 6424–6431. doi:10.1002/2015GL064694

Ryther, J. H. 1969. Photosynthesis and Fish Production in the Sea. Science **166**: 72–76. doi:10.1126/science.166.3901.72

Sarthou, G., K. R. Timmermans, S. Blain, and P. Tréguer. 2005. Growth physiology and fate of diatoms in the ocean: a review. J. Sea Res. **53**: 25–42. doi:10.1016/j.seares.2004.01.007

Schofield, O., R. A. Arnone, W. P. Bissett, T. D. Dickey, C. O. Davis, Z. Finkel, M. Oliver, and M. A. Moline. 2004. Watercolors in the coastal zone: what can we see? Oceanography 30–37.

Scott, J. D., M. A. Alexander, and D. R. Murray. 2016. The Climate Change Web Portal: a system to access and display climate and Earth system model output from the CMIP5 archive. Bulletin of the …. doi:10.1175/BAMS-D-15-00035.1

SeaWiFS Level-3 Mapped Chlorophyll Data Version 2014. Distributed Active Archive Center at NASA Goddard Space Flight Center, Ocean Ecology Laboratory, Ocean Biology Processing Group.doi:doi: 10.5067/ORBVIEW-2/SEAWIFS/L3M/CHL/2014

Seitzinger, S. P., J. A. Harrison, E. Dumont, A. H. W. Beusen, and A. F. Bouwman. 2005. Sources and delivery of carbon, nitrogen, and phosphorus to the coastal zone: An overview of Global Nutrient Export from Watersheds (NEWS) models and their application: GLOBAL EXPORT OF C, N, AND P TO COASTAL SYSTEMS. Glob. Biogeochem. Cycle **19**: n/a–n/a. doi:10.1029/2005GB002606

Shchepetkin, A. F., and J. C. McWilliams. 2005. The regional oceanic modeling system (ROMS): a split-explicit, free-surface, topography-following-coordinate oceanic model. Ocean Modelling **9**: 347–404. doi:10.1016/j.ocemod.2004.08.002

Siedlecki, S. A., I. C. Kaplan, A. J. Hermann, and others. 2016. Experiments with Seasonal Forecasts of ocean conditions for the Northern region of the California Current upwelling system. Sci. Rep. **6**: 27203. doi:10.1038/srep27203

Siedlecki, S. A., N. S. Banas, K. A. Davis, S. Giddings, B. M. Hickey, P. MacCready, T. Connolly, and S. Geier. 2015. Seasonal and interannual oxygen variability on the Washington and Oregon continental shelves. J. Geophys. Res.-Oceans **120**: 608–633. doi:10.1002/2014JC010254

Slaughter, A. M., S. M. Bollens, and G. R. Bollens. 2006. Grazing impact of mesozooplankton in an upwelling region off northern California, 2000–2003. Deep-Sea Res. Part II-Top. Stud. Oceanogr. **53**: 3099–3115.

Smayda, T. J. 1997. Harmful algal blooms: Their ecophysiology and general relevance to phytoplankton blooms in the sea. Limnol. Oceanogr. **42**: 1137–1153. doi:10.4319/lo.1997.42.5_part_2.1137

Smetacek, V. 1999. Diatoms and the Ocean Carbon Cycle. Protist **150**: 25–32.

Stewart, J. S., E. L. Hazen, D. G. Foley, and S. J. Bograd. 2012. Marine predator migration during range expansion: Humboldt squid *Dosidicus gigas* in the northern California Current System. … Ecology Progress Series. doi:10.3354/meps10022

Stock, C. A., J. G. John, R. R. Rykaczewski, and others. 2017. Reconciling fisheries catch and ocean productivity. Proc Natl Acad Sci USA **114**: E1441–E1449. doi:10.1073/pnas.1610238114

Stock, C. A., J. P. Dunne, and J. G. John. 2014. Global-scale carbon and energy flows through the marine planktonic food web: An analysis with a coupled physicalâ€“biological model. Prog. Oceanogr. **120**: 1–28. doi:10.1016/j.pocean.2013.07.001

Stock, C. A., K. Pegion, G. A. Vecchi, and others. 2015. Seasonal sea surface temperature anomaly prediction for coastal ecosystems. Prog. Oceanogr. **137 IS -**: 219–236.

Stock, C. A., M. A. Alexander, N. A. Bond, and K. M. Brander. 2011. On the use of IPCC-class models to assess the impact of climate on living marine resources. Prog. Oceanogr. **88**: 1–27. doi:10.1016/j.pocean.2010.09.001

Stock, C. A., T. M. Powell, and S. A. Levin. 2008. Bottom–up and top–down forcing in a simple size-structured plankton dynamics model. J. Mar. Syst. **74**: 134–152.
Stock, C., and J. Dunne. 2010. Controls on the ratio of mesozooplankton production to primary production in marine ecosystems. Deep-Sea Res. Part I-Oceanogr. Res. Pap. **57**: 95–112. doi:10.1016/j.dsr.2009.10.006
Stolte, W., and R. Riegman. 1995. Effect of phytoplankton cell-size on transient-state nitrate and ammonium uptake kinetics. Microbiology-Uk **141**: 1221–1229.
Stukel, M. R., and M. D. Ohman. 2013. Contributions of mesozooplankton to vertical carbon export in a coastal upwelling system. Marine Ecology …. doi:10.3354/meps10453
Stukel, M. R., L. I. Aluwihare, and K. A. Barbeau. 2017. Mesoscale ocean fronts enhance carbon export due to gravitational sinking and subduction. Proceedings of the Proceedings of the ….
Sunda, W. G., and S. A. Huntsman. 1995. Iron uptake and growth limitation in oceanic and coastal phytoplankton. Mar. Chem. **50**: 189–206. doi:10.1016/0304-4203(95)00035-P
Sunda, W. G., and S. A. Huntsman. 1997. Interrelated influence of iron, light and cell size on marine phytoplankton growth. Nature **390**: 389–392.
Tang, E. P. Y. 1995. The allometry of algal growth-rates. J. Plankton Res. **17**: 1325–1335. doi:10.1093/plankt/17.6.1325
Taylor, A. G., M. R. Landry, K. E. Selph, and J. J. Wokuluk. 2015. Temporal and spatial patterns of microbial community biomass and composition in the Southern California Current Ecosystem. Deep-Sea Res. Part II-Top. Stud. Oceanogr. **112**: 117–128. doi:10.1016/j.dsr2.2014.02.006
Taylor, A. G., R. Goericke, M. R. Landry, K. E. Selph, D. A. Wick, and M. J. Roadman. 2012. Sharp gradients in phytoplankton community structure across a frontal zone in the California Current Ecosystem. J. Plankton Res. **34**: 778–789. doi:10.1093/plankt/fbs036
Terseleer, N., J. Bruggeman, C. Lancelot, and N. Gypens. 2014. Trait-based representation of diatom functional diversity in a plankton functional type model of the eutrophied southern North Sea. Limnol. Oceanogr. **59**: 1958–1972. doi:10.4319/lo.2014.59.6.1958
Thingstad, F. T. 1998. A theoretical approach to structuring mechanisms in the pelagic food web. Hydrobiologia **363**: 59–72.
Tommasi, D., C. A. Stock, A. J. Hobday, and others. 2017. Managing living marine resources in a dynamic environment: The role of seasonal to decadal climate forecasts. Prog. Oceanogr. **152**: 15–49.
Tremblay, J.-E., B. Klein, L. Legendre, R. B. Rivkin, and J.-C. Therriault. 1997. Estimation of f-ratios in oceans based on phytoplankton size structure. Limnol. Oceanogr. **42**: 595–601. doi:10.4319/lo.1997.42.3.0595
Uitz, J., H. Claustre, B. Gentili, and D. Stramski. 2010. Phytoplankton class-specific primary production in the world's oceans: Seasonal and interannual variability from satellite observations. Glob. Biogeochem. Cycle **24**. doi:10.1029/2009gb003680
Van Oostende, N., J. P. Dunne, S. E. Fawcett, and B. B. Ward. 2015. Phytoplankton succession explains size-partitioning of new production following upwelling-induced blooms. Journal of Marine Systems **148**: 14–25. doi:10.1016/j.jmarsys.2015.01.009
Venrick, E. L. 2002. Floral patterns in the California current system off southern California: 1990-1996. J. Mar. Res. **60**: 171–189. doi:10.1357/002224002762341294
Venrick, E. L. 2009. Floral patterns in the California Current: The coastal-offshore boundary zone. J. Mar. Res. **67**: 89–111.

Vidussi, F., H. Claustre, B. B. Manca, A. Luchetta, and J. C. Marty. 2001. Phytoplankton pigment distribution in relation to upper thermocline circulation in the eastern Mediterranean Sea during winter. Journal of Geophysical Research: Oceans **106**: 19939–19956. doi:10.1029/1999JC000308

Waite, A. M., P. A. Thompson, and P. J. Harrison. 1992a. Does energy control the sinking rates of marine diatoms? Limnol. Oceanogr. **37**: 468–477. doi:10.4319/lo.1992.37.3.0468

Waite, A., P. K. Bienfang, and P. J. Harrison. 1992b. Spring bloom sedimentation in a subarctic ecosystem. Mar. Biol. **114**: 119–129. doi:10.1007/BF00350861

Ward, B. A., and M. J. Follows. 2016. Marine mixotrophy increases trophic transfer efficiency, mean organism size, and vertical carbon flux. … of the National Academy of Sciences. doi:10.1073/pnas.1517118113

Ward, B. A., E. Marañón, and B. Sauterey. 2017. The Size Dependence of Phytoplankton Growth Rates: A Trade-Off between Nutrient Uptake and Metabolism. The American …. doi:10.1086/689992

Ward, B. A., S. Dutkiewicz, and O. Jahn. 2012. A size-structured food-web model for the global ocean. Limnology and …. doi:10.4319/lo.2012.57.6.1877

West, G. B. 1997. A general model for the origin of allometric scaling laws in biology. Science **276**: 122–126. doi:10.1126/science.276.5309.122

Wheeler, P. A., and A. Huyer. 2003. Cold halocline, increased nutrients and higher chlorophyll off Oregon in 2002. Geophysical Research …. doi:10.1029/2003GL017395

Wilkerson, F. P., R. C. Dugdale, R. M. Kudela, and F. P. Chavez. 2000. Biomass and productivity in Monterey Bay, California: contribution of the large phytoplankton. Deep-Sea Res. Part II-Top. Stud. Oceanogr. **47**: 1003–1022. doi:10.1016/S0967-0645(99)00134-4